

Characterization of Stainless Steel and Refractory Metal Welds Made Using a Diode- Pumped, Continuous Wave Nd: YAG Laser

*T. A. Palmer, B. Wood, J. W. Elmer, C. Westrich, J. O.
Milewski, M. Piltch, M. Barbe, R. Carpenter*

October 19, 2001

U.S. Department of Energy

Lawrence
Livermore
National
Laboratory

DISCLAIMER

This document was prepared as an account of work sponsored by an agency of the United States Government. Neither the United States Government nor the University of California nor any of their employees, makes any warranty, express or implied, or assumes any legal liability or responsibility for the accuracy, completeness, or usefulness of any information, apparatus, product, or process disclosed, or represents that its use would not infringe privately owned rights. Reference herein to any specific commercial product, process, or service by trade name, trademark, manufacturer, or otherwise, does not necessarily constitute or imply its endorsement, recommendation, or favoring by the United States Government or the University of California. The views and opinions of authors expressed herein do not necessarily state or reflect those of the United States Government or the University of California, and shall not be used for advertising or product endorsement purposes.

This work was performed under the auspices of the U. S. Department of Energy by the University of California, Lawrence Livermore National Laboratory under Contract No. W-7405-Eng-48.

This report has been reproduced directly from the best available copy.

Available electronically at <http://www.doc.gov/bridge>

Available for a processing fee to U.S. Department of Energy
And its contractors in paper from
U.S. Department of Energy
Office of Scientific and Technical Information
P.O. Box 62
Oak Ridge, TN 37831-0062
Telephone: (865) 576-8401
Facsimile: (865) 576-5728
E-mail: reports@adonis.osti.gov

Available for the sale to the public from
U.S. Department of Commerce
National Technical Information Service
5285 Port Royal Road
Springfield, VA 22161
Telephone: (800) 553-6847
Facsimile: (703) 605-6900
E-mail: orders@ntis.fedworld.gov
Online ordering: <http://www.ntis.gov/ordering.htm>

OR

Lawrence Livermore National Laboratory
Technical Information Department's Digital Library
<http://www.llnl.gov/tid/Library.html>

**Characterization of Stainless Steel and Refractory Metal Welds Made
Using a Diode-Pumped, Continuous Wave Nd:YAG Laser**

T.A. Palmer, B. Wood, J.W. Elmer, and C. Westrich
Lawrence Livermore National Laboratory
Livermore, CA

J.O. Milewski, M. Piltch, M. Barbe, and R. Carpenter
‡ Los Alamos National Laboratory
Los Alamos, NM

Abstract

A series of laser welds have been made on several materials using a Rofin-Sinar DY-033, 3.3 kW, Diode-Pumped Continuous Wave (CW) Nd:YAG laser system, located at Los Alamos National Laboratory. Materials welded in these experiments include 21-6-9 stainless steel, 304L stainless steel, vanadium, and tantalum. The effects of changes in the power input at a constant travel speed on the depth, width, aspect ratio, and total melted area of the welds have been analyzed. Increases in the measured weld pool dimensions as a function of power input are compared for each of the base metals investigated. These results provide a basis for further examining the characteristics of diode pumped CW Nd:YAG laser systems in welding applications.

Introduction

High-power, pulsed Nd:YAG lasers have long been available for industrial welding applications. The recent development of kilowatt-range continuous-wave (CW) Nd:YAG lasers, which deliver a high energy beam to the material continuously rather than in discrete pulses, may provide several advantages over pulsed systems. For example, the steady beam behavior exhibited by CW systems allows for greater travel speeds, as they are not limited by pulse rate and pulse overlap, to achieve exacting weld dimensions in high-precision applications.

Diode-pumped lasers also offer greater flexibility and reliability over their traditional flash lamp pumped counterparts. Diode lifetimes are long and the diode modules are easily replaceable upon failure, thus keeping laser down-time to a minimum. Beam quality in such systems is generally superior to that obtained by lamp pumping, due to pumping at the high absorption wavelengths of the laser rod, which reduces heat and thermal lensing of the rod. This feature allows for tighter beam control and higher energy densities due to the smaller focal spot sizes, resulting in faster travel speeds. Diode pumping is also more efficient, which reduces the footprint of the system and requires less power to operate. The output of such diode-pumped CW Nd:YAG lasers can also be introduced, via small diameter fibers, into a controlled operating environment, such as an atmospheric chamber.

The objective of this report is to determine the exact behavior of one such diode-pumped cw Nd:YAG laser welding system—a 3.3 kW Rofin Sinar DY-033 currently installed and operating at Los Alamos National Laboratory—on various materials, in preparation for the installation of a similar system (the 2.2 kW model) at Lawrence Livermore National Laboratory. In particular, we wish to examine how the resulting depth, width, and weld geometry vary with power, incident beam angle for welding refractory metals, and changes in the shielding gas. As a secondary goal, we have evaluated the Los Alamos system for its ease of use and its overall robustness.

Experimental

A Rofin-Sinar DY-033, 3.3 kW, diode pumped cw Nd:YAG laser, located at Los Alamos National Laboratory, has been used to produce welds on several materials, including 304L stainless steel, 21-6-9 stainless steel, vanadium (with 0.0340 wt.% Si, 0.0052 wt.% C, 0.0004 wt.% H, 0.0170 wt.% N, and 0.0100 wt.% O), and tantalum (< 0.002 wt.% C, < 0.0003 wt.% H, < 0.002 wt.% N, and < 0.0050 wt.% O). The chemical compositions of the two stainless steels

used in these experiments are given in Table 1, and a summary of the physical properties of each material is given in Table 2. The output beam of the Rofin Sinar DY-033 is delivered through a 400 μm fiber, collimated using a 120 mm focal-length collimating lens, and subsequently passed through a 160 mm focal-length focusing lens. After traveling through this optics path, the laser spot size is calculated to be approximately 530 μm in diameter. Each weld is made with the laser spot focused on the surface of the sample.

Weld coupons 6 inches in length, 0.4 inch in width, and 0.120 inch in thickness, except the tantalum samples, which are 0.130 inch thick, are used here. A step joint equal to 50% of the sample thickness has also been machined along the length of one side of each welding coupon in order to create a step geometry for the butt weld joint. A schematic diagram of the cross section of the joint geometry is shown in Figure 1, showing where the laser beam contacts the material surface and the relative location of the step with respect to the laser spot.

Three welds, each 1.5" in length, are made on each set of weld coupons. Shielding of the weld pool is provided by the delivery of argon or helium across the sample surface. Constant flow rates of 90 cfh for the helium and 30 cfh for the argon have been used. In addition to the shielding, a portable HEPA filtering system is used for fume extraction. The effects of changes in the power, shielding gas, and incident angle of the laser beam on the sample on the resulting weld pool shape and size have been investigated. Table 3 gives an overview of the various welding parameters used for each material. Since the stainless steel and vanadium samples have been welded under nearly identical conditions, except for a difference in the head tilt angle, they are considered together here.

The tantalum samples have been welded under conditions different from those used in the other samples, making the results not easily comparable with the other materials. Refractory metals, such as tantalum, display high melting points and relatively high powers are required to weld in a conduction mode of melting. Back reflections of the laser light off the molten pool surface could damage the delivery optics. Therefore, during the welding of the vanadium and tantalum samples, the head of the laser has been tilted at angles of 10° and 20° as a precautionary measure. The inclusion of this tilt, which is not necessary in full penetration or deep keyhole mode welding or in the welding of the stainless steel samples, helps to alleviate this concern at the power levels studied here.

After welding, cross sectional samples have been cut from each weld, mounted, polished, and etched using standard metallographic procedures. The 21-6-9 and 304L stainless steel samples have been etched using an electrolytic oxalic acid etch, while the vanadium and several of the tantalum samples have been etched using a glycerol-HF-HNO₃ solution. Several other tantalum samples have been etched using a water-ammonium bifluoride-HNO₃ solution. This second etchant has been used on tantalum samples when the first glycerol etchant proved insufficient in bringing out the desired microstructure. In each case, the etchant has been used to reveal the fusion zone of each weld in order that its size and shape could be quantified. Measurements of the depth of penetration, the width at the top surface, the aspect ratio (depth/width), and the total melted area are then made on each weld cross section using a commercial image analysis software package (Image Pro Plus, v. 4.1, Media Cybernetics, Inc., Silver Spring, MD).

Results and Discussion

Stainless Steel and Vanadium Welds

The measurements made on the stainless steel and vanadium samples welded at a travel speed of 45 in/min with helium and argon shielding are shown in Tables 4 and 5, respectively. In each table, the weld depth, width at the top surface, aspect ratio (defined here as depth/width), and the total melted area are shown for each power setting along with a brief description of the weld cross section. Micrographs of the weld cross section and the weld surface for each weld are shown in Appendices I to III.

Each observed cross section can be described as either a conduction mode, a keyhole mode, or a full penetration (through thickness) weld. For the 21-6-9 stainless steel, keyhole penetration dominates at powers above 500 W, for both a helium and argon shielding gas. A full penetration weld is observed at powers of 1250 and 1500 W. Similar behavior is observed with the 304L weld samples, except that a full penetration weld is not made with powers less than 1500 W. On the other hand, the vanadium weld samples prove to be much harder to melt. In fact, at 250 W, only the surface of the vanadium sample is melted, leaving no discernible weld pool, and a keyhole penetration is not observed below a power setting of 1000 W. A full penetration weld is not formed until a power setting of 2250 W, which is significantly higher than the powers required for the stainless steel samples, is reached.

Further examination of the weld cross sections from each material reveals the presence of porosity in several of the welds. The porosity primarily appears in the 304L and vanadium samples at higher powers. For example, porosity appears in the 304L samples at powers above 1000 W with a helium shielding gas and 750 W with an argon shielding gas. These welds are either keyhole mode or full penetration, and the porosity appears primarily near the bottom of the keyhole. In the vanadium samples, porosity appears at powers above 1250 W. Like the 304L welds, these welds are either keyhole mode or full penetration welds, and the porosity primarily appears in the region near the bottom of the keyhole. On the other hand, the 21-6-9 samples display little porosity at a laser power of 750 W with a helium shielding gas, where porosity is observed near the bottom of the keyhole. Since this study is not concerned with porosity formation in these alloys, the mechanisms governing porosity formation in the various alloys are not considered here.

Comparisons of the weld depth and width measurements for each material and power setting using helium as the shielding gas and at a travel speed of 45 in/min are shown in Figures 2 and 3, respectively. Rather significant differences in the behavioral trends of the width and depth with increases in the power are observed in these figures. For example, the three materials show a consistent increase in the measured weld depth with increasing power until the depth reaches the thickness of the welding coupon in Figure 2. Of the three materials examined in this figure, the 21-6-9 stainless steel samples show the greatest depths at each power setting, followed by the 304L stainless steel and the vanadium welds. On the other hand, the variation in weld width with increasing power does not display a similarly consistent trend. As shown in Figure 3, only the vanadium samples demonstrate a consistent increase in the weld width with increasing power. The weld widths measured in the stainless steel samples level out and even decreases at the higher power levels where full penetration welds are made. A comparison with the 21-6-9 welds also shows that these welds become much wider than the 21-6-9 welds at the higher powers where full penetration welds are observed.

Measurements of the weld depth and width have also been made for samples welded using an argon shielding gas at different power levels with a travel speed of 45 in/min. Figures 4 show these measurements as a function of power for the two stainless steel and vanadium welds. Even though a rather narrow power range is examined, trends similar to those observed with a helium shielding gas are also present with argon. In Figure 4, which shows the weld depth as a function of power, the depth increases with increasing power for all three materials, with the 21-6-9

showing the greatest depth. The weld width also increases with increasing power, as shown in Figure 5. Like the observations made with a helium shielding gas, the 304L welds display a greater width than the 21-6-9 and vanadium welds. In fact, a comparison of the weld widths and depths for both helium and argon shielding gases in Tables 4 and 5, shows that there is little difference between these values, indicating that the choice of shielding gas may have little effect on the resulting weld size.

In addition to measurements of the weld width and depth, the aspect ratio, represented as the depth to width ratio, and the total melted area of each weld have been measured. Examination of these parameters provides more information concerning the general shape of the weld pool and the melting efficiency of the laser at the various power settings. Figures 6 and 7 show the measured aspect ratios and areas of each weld as a function of power with helium shielding gas. As shown in each figure, the general trends for the aspect ratio and total melted area are not as drastically affected by the weld reaching full penetration as the depth and width have been.

Both the aspect ratio and the total melted area of each material generally increase with increasing power. The 21-6-9 stainless steel samples display the greatest depth/width ratio over the entire range of powers, reaching to a depth twice that of the measured width at 1500 W. Even though several vanadium samples have been welded at higher powers than stainless steels, the aspect ratios, even at a power of 2250 W, are far below those measured in the stainless steels. The same is not true for the observed trends in the total area of the weld pool as a function of power. At powers below 1500 W, the areas of the stainless steel samples consistently exceed those of the vanadium welds. With increasing power levels up to 2250 W, the areas of the vanadium welds continue to increase to levels nearly 1.5 times that observed in the stainless steels.

Figures 8 and 9 show the aspect ratios and melted areas of each weld with an argon shielding gas. Even though the power distribution over which the measurements are made is much smaller than that for the helium shielding gas conditions, the same general trends observed previously are also present here. For example, the aspect ratio-power relationships, shown in Figure 8, closely resemble that observed in Figure 6. The aspect ratio and total melted area for each material show a general increase over the range of powers analyzed, and the 21-6-9 welds display the highest depth/width ratios and total melted areas over the range of powers analyzed. On the other hand, the vanadium welds show a much smaller aspect ratio at the lower powers with the

argon shielding gas when compared with the helium shielding gas. As the power is increased, the values converge.

Tantalum Welds

In addition to the 21-6-9 and 304L stainless steel and vanadium welds described above, tantalum samples with the same sample geometry have been welded. Micrographs of the top surface and cross section of each weld are shown in Appendix IV. Measurements similar to those described above have also been made on a series of tantalum welds made with different laser tilt angles, travel speeds, shielding gases, and power inputs. A summary of these measurements and welding conditions along with a description of each weld cross section is given in Table 6. It is apparent from both the micrographs in Appendix IV and the measurements of the weld cross sections that higher powers are required to achieve weld pool dimensions similar to the above materials. For example, over the power levels tested here, no tantalum weld displays full penetration, which is observed at the higher power levels for the other three materials. In addition, a keyhole mode weld is not observed in the tantalum samples below powers of 1500 W. Even then, the keyhole shape in the weld pool cross section is not as well defined as that observed in the stainless steel welds.

An examination of the weld cross sections and top surfaces in Appendix IV for each welding condition shows porosity and a degree of undercutting in the tantalum welds at powers above 1000 W with a 10 head tilt and a 30 in/min travel speed with helium shielding. The porosity appears primarily near the root of the weld, in both conduction mode (1000 W) and keyhole mode welds. These same welds also show undercutting on the top surface of the welds. In addition to the porosity and undercutting, there is also a significant amount of cracking present in the weld cross section at a power of 1750 W. The other welding conditions studied here display much different characteristics. With a 20° head tilt at this travel speed, there is no visible porosity in the weld cross section below a power of 2000 W. As the travel speed is increased to 45 in/min, no porosity is observed at either tilt angle or shielding gas or over the range of powers.

The effects of changes in the tilt angle on the weld depth, width, aspect ratio, and total melted area at a travel speed of 30 in/min are shown in Figures 10 to 13. Measurements taken at each tilt angle shows a general increase as the power is increased, much like the conditions observed with the stainless steel and vanadium samples. On the other hand, the magnitudes of each of the

measurements on the tantalum welds are on the same level as the vanadium welds, which are much below the values measured in the stainless steel welds. Overall, there is little difference between the measurements made at each tilt angle. Therefore, it is apparent that the change in tilt angle has a rather minimal effect on the resulting weld properties, at least at this slower travel speed. When a more rapid travel speed of 45 in/min is attempted, the tilt angle has a more marked effect on the resulting weld pool dimensions. For example, no melting is observed with a head tilt of 20° with powers of up to 3 kW. With a 10° head tilt, though, melting of the tantalum is observed.

The effects of changes in the shielding gas at a single tilt angle and a travel speed of 45 in/min on the relationships between the weld depth, width, aspect ratio, and total melted area are shown in Figures 14 to 17, respectively. Even though the range of powers analyzed is rather limited, there is a general increase in the size of the weld parameters with an increase in power, albeit rather small. Overall, there is little difference between the measurements made with an argon or helium shielding gas, indicating that there is also a minimal effect of the shielding gas choice on the resulting weld at a given power.

Summary and Conclusions

A series of welds have been made on 21-6-9, 304L, vanadium, and tantalum samples using a 3.3 kW CW Nd:YAG laser. Measurements of the weld depth, width, aspect ratio (depth/width ratio), and the total melted area are reported here for these materials over a range of powers and for helium and argon shielding gases. All of the materials discussed here are weldable, to a varying degree, with this cw Nd:YAG laser. Each material, though, displays a transition from conduction to keyhole modes at different power density levels. Of these materials, the 21-6-9 stainless steel transitions to a keyhole mode and full penetration at the lowest power levels, while tantalum displays the highest powers for this transition and never reaches full penetration. Reasons for these differences in weld pool shape and size between these materials have not been pursued here but require further study in the future.

Analysis of the measurements of the weld pool cross sections, including the weld width, depth, aspect ratio, and total melted area, shows that increases in power result in increases in these weld pool dimensions. Of the weld dimensions studied, the aspect ratio (depth/width) and the total melted area display the most consistent trends and are least affected when the weld

reaches full penetration. Changes in weld parameters other than power, to include the shielding gas choice and the head tilt angle for tantalum, appear to have little to no effect on the resulting weld pool dimensions.

Acknowledgments

The authors would like to thank G.F. Ellsworth for making the measurements on the weld cross samples, R. Vallier and V. Mason-Reed for the metallographic preparation of the samples, G. Gallegos for providing the vanadium for these studies, and W. Bish for providing the stainless steel and tantalum.

References

1. E.A. Brandes (Ed.): Smithells Metals Reference Book, Seventh Edition, 1992, London, Butterworth and Heinemann.
2. J.W. Elmer, W.H. Geidt, and T.W. Eagar, "The Transition from Shallow to Deep Penetration During Electron Beam Welding," *Weld. J. Res. Suppl.*, 69(5), 167s-176s.
3. Filing Code: SS-327, Alloy Digest, (Engineering Alloys Digest, Inc., Upper Montclair, NJ), 1990.
4. Filing Code: SS-254, Alloy Digest, (Engineering Alloys Digest, Inc., Upper Montclair, NJ), 1971.

Table 1. Chemical compositions of the 21-6-9 Stainless Steel and the 304L Stainless Steel.

	<u>21-6-9</u>	<u>304L</u>
<u>Element</u>	<u>Chemical Composition</u> <u>(wt.%)</u>	<u>Chemical Composition</u> <u>(wt.%)</u>
Fe	Bal.	BAL
Cr	18.9	18.3
Ni	7.4	8.7
Mn	8.8	1.9
C	0.0342	0.0218
Si	0.4660	0.4780
Sn	0.2100	0.1800
V	0.1660	0.0660
Cu	0.1600	0.2770
Mo	0.1020	0.2560
Co	0.0770	0.0940
Nb	0.0300	< 0.0100
W	0.0200	0.0600
Al	0.0140	< 0.0100
P	< 0.0100	0.0200
N	0.2600	0.0760
O	< 0.0050	< 0.0050
H	0.0003	< 0.0003

Table 2. Summary of physical properties of materials used in this study.¹⁻³

<u>Material</u>	<u>Melting Point (°C)</u>	<u>Boiling Point (°C)</u>	<u>Vapor Pressure (Pa)*</u>	<u>Heat Capacity * (J/gm-K)</u>	<u>Thermal Conductivity * (W/mm-K)</u>
304L Stainless Steel	1433	---	---	0.5*	0.025*
21-6-9 Stainless Steel	---	---	---	---	0.0268***
Vanadium	1902	3410	5.4582×10^{-10}	0.6607	0.0352**
Tantalum	2980	5370	1.28016×10^{-11}	0.1325	0.054#

* Average value at temperature halfway between room temperature and the melting point.

** Value at 700°C.

*** Value at 760°C.

Value at 100°C.

Table 3. Summary of welding parameters.

<u>Material</u>	<u>Number of Welds</u>	<u>Power Range (W)</u>		<u>Travel Speed (in/min)</u>	<u>Shielding Gas</u>	<u>Shielding Gas Flow Rate (cfh)</u>	<u>Laser Head Tilt (degrees)</u>
		<u>Min</u>	<u>Max</u>				
21-6-9 SS	6	250	1500	45	He	90	0
	3	750	1250	45	Ar	30	0
304L SS	6	250	1500	45	He	90	0
	3	750	1250	45	Ar	30	0
Vanadium	9	250	2250	45	He	90	10
	3	750	1250	45	Ar	30	10
Tantalum	4	500	2000	30	He	150	20
	5	500	2000	30	He	150	10
	3	250	1250	45	He	90	10
	3	750	1250	45	Ar	30	10

Table 4. Summary of weld dimension measurements for samples welded with He shielding gas and at a travel speed of 45 in/min. Vanadium samples are welded with a 10° incident angle between the laser beam and the sample surface.

	<u>Power (W)</u>	<u>General Description</u>	<u>Weld Depth (mm)</u>	<u>Width at Top Surface (mm)</u>	<u>Aspect Ratio (Depth/Width)</u>	<u>Total Melted Area (mm²)</u>
21-6-9 SS	250	Conduction	0.138	0.578	0.239	0.057
	500	Keyhole	1.004	1.211	0.829	0.603
	750	Keyhole	1.924	1.406	1.368	1.337
	1000	Keyhole	2.663	1.484	1.795	2.078
	1250	Through Thickness	2.933	1.490	1.969	2.653
	1500	Through Thickness	2.950	1.383	2.133	2.805
304 L SS	250	Conduction	0.124	0.576	0.215	0.054
	500	Keyhole	0.825	1.197	0.689	0.538
	750	Keyhole	1.538	1.467	1.049	1.172
	1000	Keyhole	2.047	1.409	1.453	1.768
	1250	Keyhole	2.433	1.755	1.386	2.354
	1500	Through Thickness	2.818	1.832	1.538	3.254
Vanadium	250	Surface Melt	---	---	---	---
	500	Conduction	0.213	0.598	0.357	0.095
	750	Conduction	0.853	1.170	0.729	0.681
	1000	Keyhole	1.170	1.378	0.849	1.002
	1250	Keyhole	1.469	1.671	0.808	1.669
	1500	Keyhole	1.865	1.902	0.981	2.295
	1750	Keyhole	2.207	2.232	0.989	3.162
	2000	Keyhole	2.481	2.384	1.041	4.181
	2250	Through Thickness	3.005	2.542	1.182	5.149

Table 5. Summary of weld dimension measurements for samples welded with an Ar Shielding gas and at a travel speed of 45 in/min.

	<u>Power (W)</u>	<u>General Description</u>	<u>Weld Depth (mm)</u>	<u>Width at Top Surface (mm)</u>	<u>Aspect Ratio (Depth/Width)</u>	<u>Total Melted Area (mm²)</u>
21-6-9 SS	750	Keyhole	2.001	1.340	1.493	1.355
	1000	Keyhole	2.427	1.363	1.781	2.016
	1250	Through Thickness	2.945	1.455	2.024	2.421
304 L SS	750	Keyhole	1.415	1.619	0.874	1.211
	1000	Keyhole	1.898	1.793	1.058	1.797
	1250	Keyhole	2.234	1.920	1.164	2.206
Vanadium	750	Conduction	0.206	0.906	0.227	0.123
	1000	Conduction	0.412	1.171	0.352	0.356
	1250	Keyhole	1.288	1.594	0.808	1.567

Table 6. Summary of weld pool dimension measurements for tantalum samples.

<u>Power (W)</u>	<u>Shielding Gas</u>	<u>Travel Speed (in/min)</u>	<u>Incident Angle (degrees)</u>	<u>General De- scription</u>	<u>Weld Depth (mm)</u>	<u>Width at Top Surface (mm)</u>	<u>Aspect Ratio (Depth/Width)</u>	<u>Total Melted Area (mm²)</u>
500	He	30	20	Surface Melt	---	---	---	---
1000	He	30	20	Conduction	0.594	1.188	0.500	0.372
1500	He	30	20	Keyhole	1.382	2.153	0.642	1.523
2000	He	30	20	Keyhole	2.165	2.071	1.045	2.682
500	He	30	10	Conduction	0.100	0.336	0.298	0.027
1000	He	30	10	Conduction	0.471	0.471	0.953	0.494
1500	He	30	10	Keyhole	1.576	1.612	0.978	1.480
1750	He	30	10	Keyhole	1.776	1.777	1.000	2.020
2000	He	30	10	Keyhole	2.200	2.436	0.903	2.891
250	He	45	10	Surface Melt	---	---	---	---
750	He	45	10	Conduction	0.133	0.594	0.222	0.062
1250	He	45	10	Conduction	0.852	1.037	0.822	0.682
750	Ar	45	10	Conduction	0.125	0.456	0.275	0.053
1000	Ar	45	10	Conduction	0.198	0.594	0.336	0.106
1250	Ar	45	10	Conduction	0.879	1.125	0.781	0.821

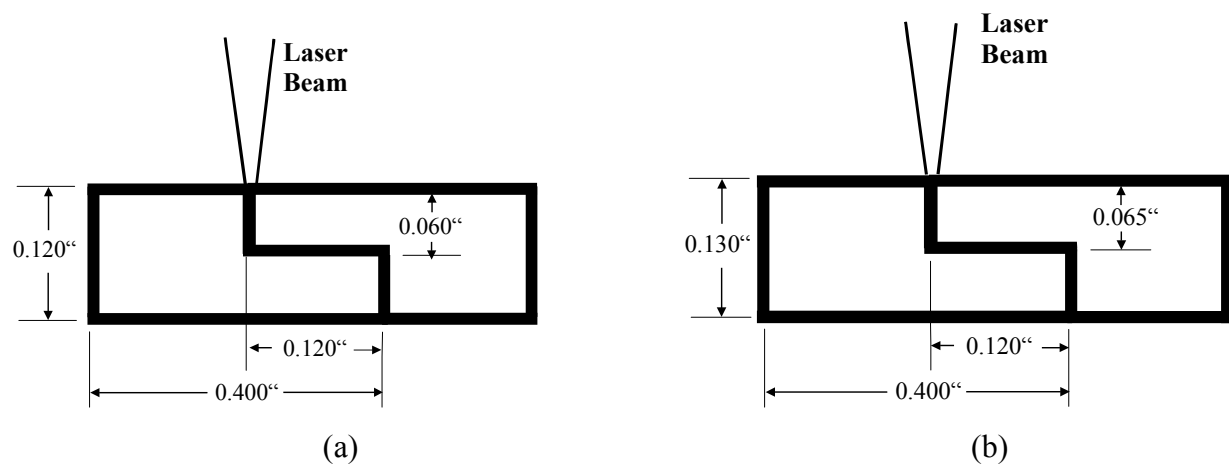


Figure 1. Schematic diagrams of the sample geometry cross section for the (a) stainless steel and vanadium samples and the (b) tantalum samples.

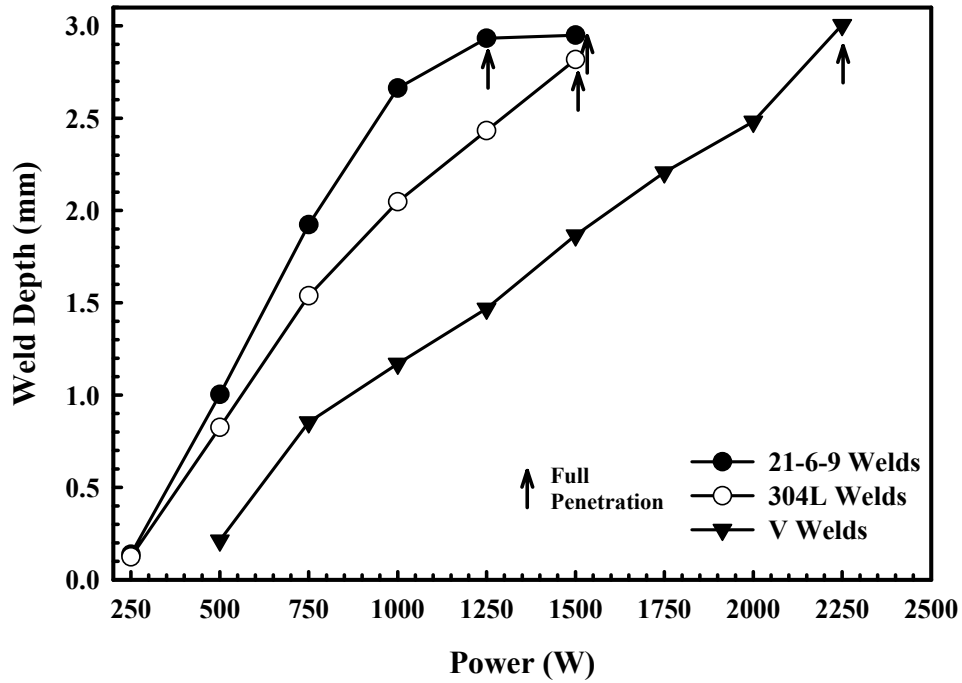


Figure 2. Comparison between measured depths of penetration for weld samples with He shielding gas and a travel speed of 45 in/min.

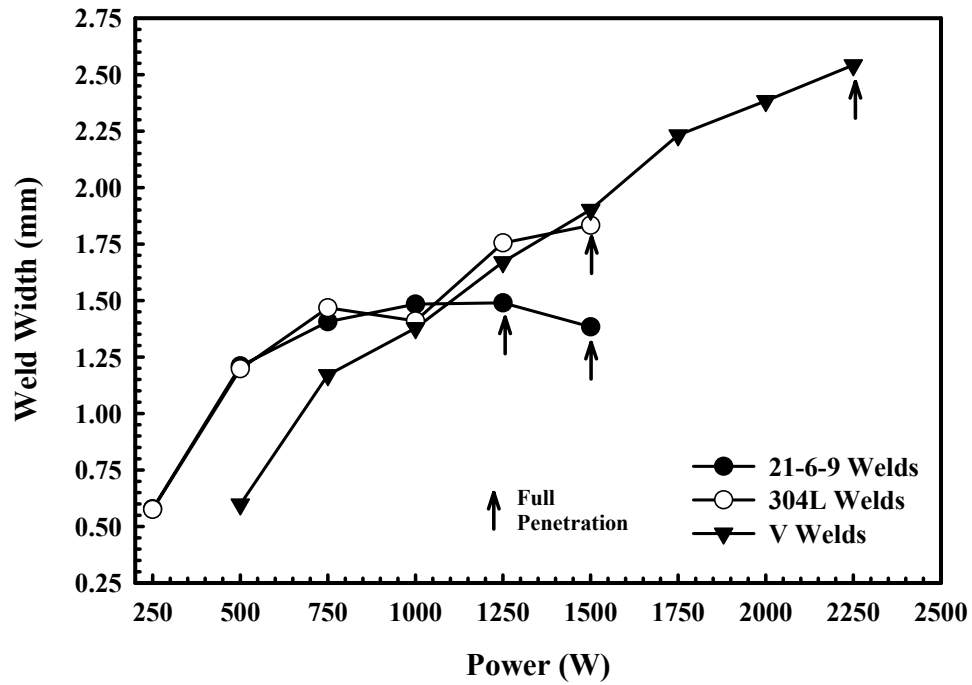


Figure 3. Comparison between measured widths for weld samples with He shielding gas and a travel speed of 45 in/min.

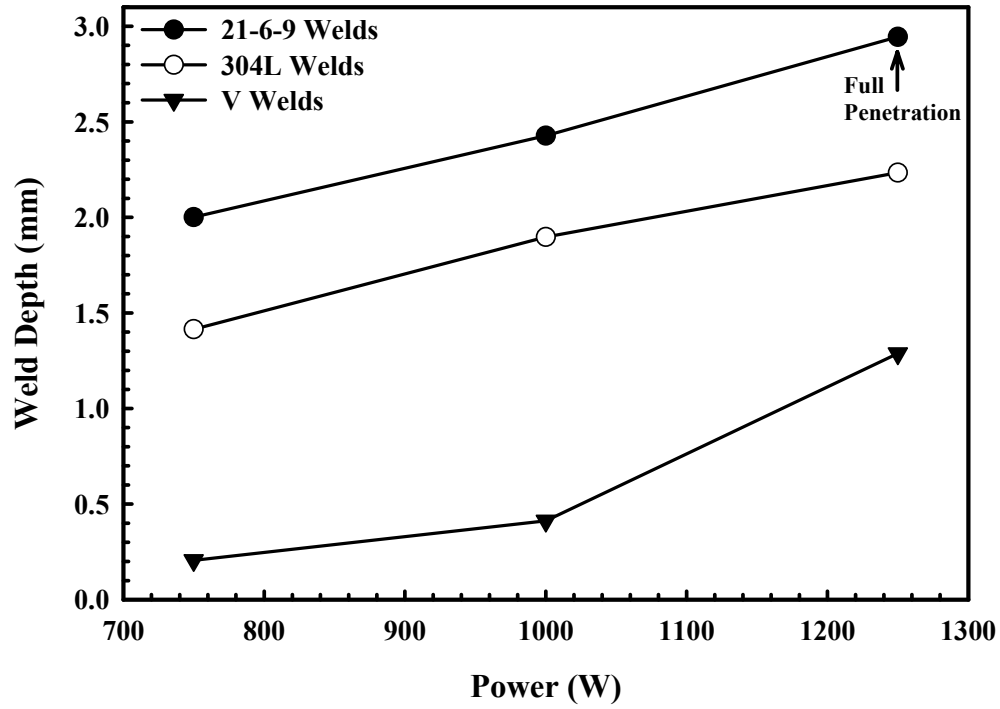


Figure 4. Comparison between measured depths of penetration for weld samples with Ar shielding gas and a travel speed of 45 in/min.

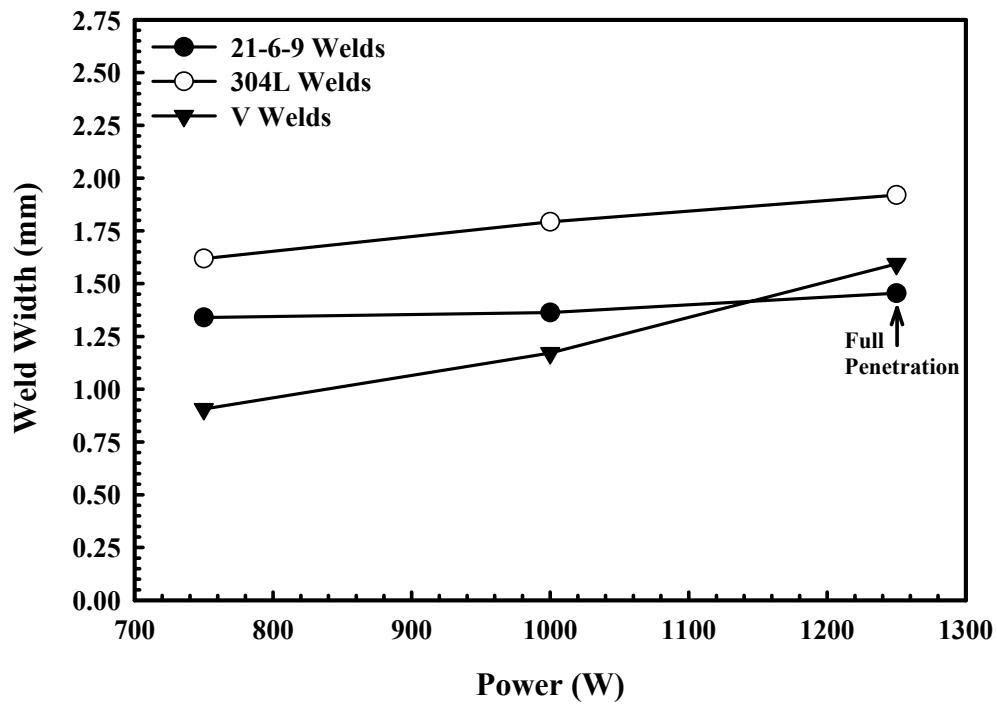


Figure 5. Comparison between measured widths for weld samples with Ar shielding gas and a travel speed of 45 in/min.

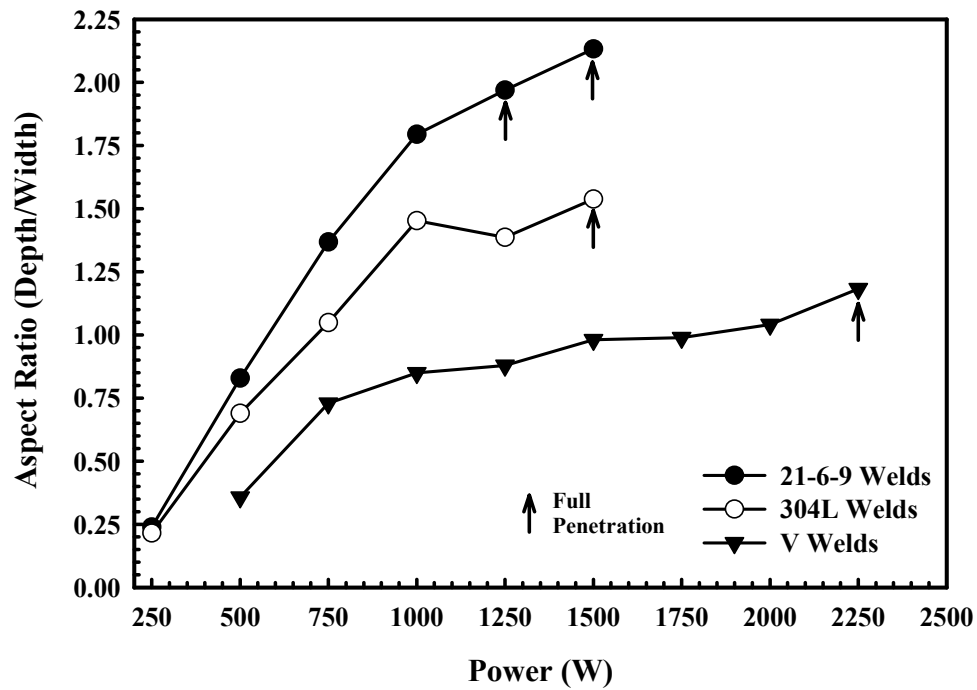


Figure 6. Comparison between the aspect ratios (depth/width) for weld samples with He shielding gas and a travel speed of 45 in/min.

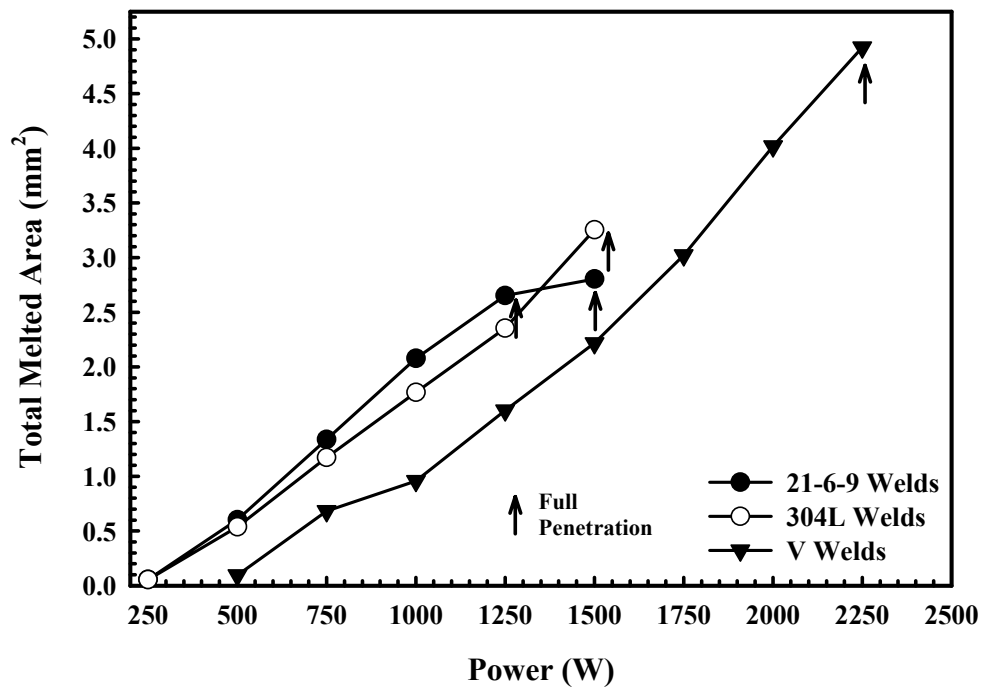


Figure 7. Comparison between total melted area (mm²) for weld samples with He shielding gas and a travel speed of 45 in/min.

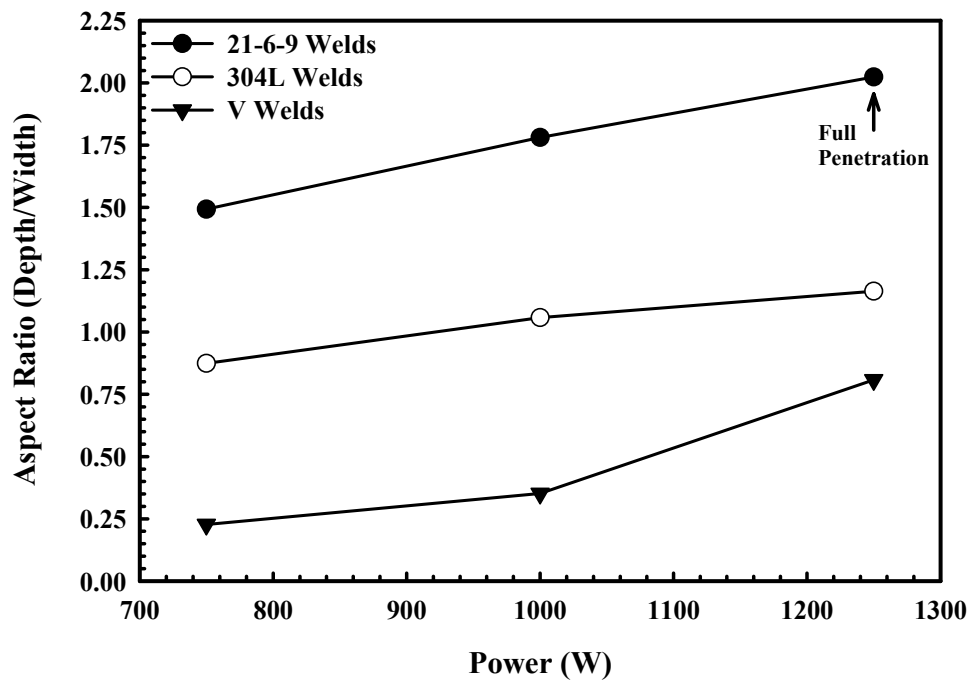


Figure 8. Comparison between the aspect ratios (depth/width) for weld samples with Ar shielding gas and a travel speed of 45 in/min.

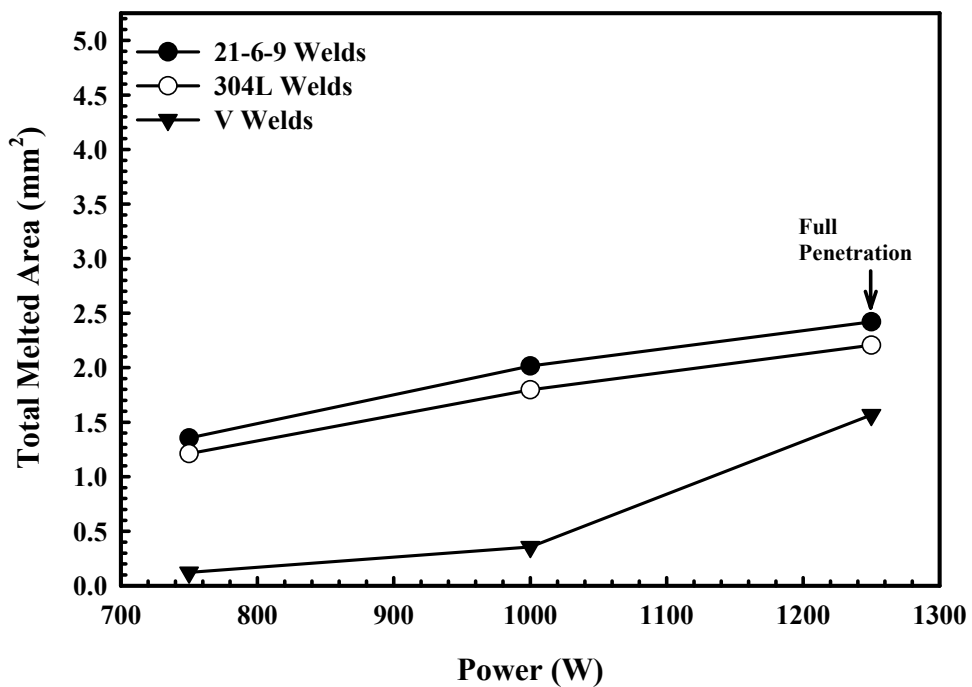


Figure 9. Comparison between total melted area (mm²) for weld samples with Ar shielding gas and a travel speed of 45 in/min.

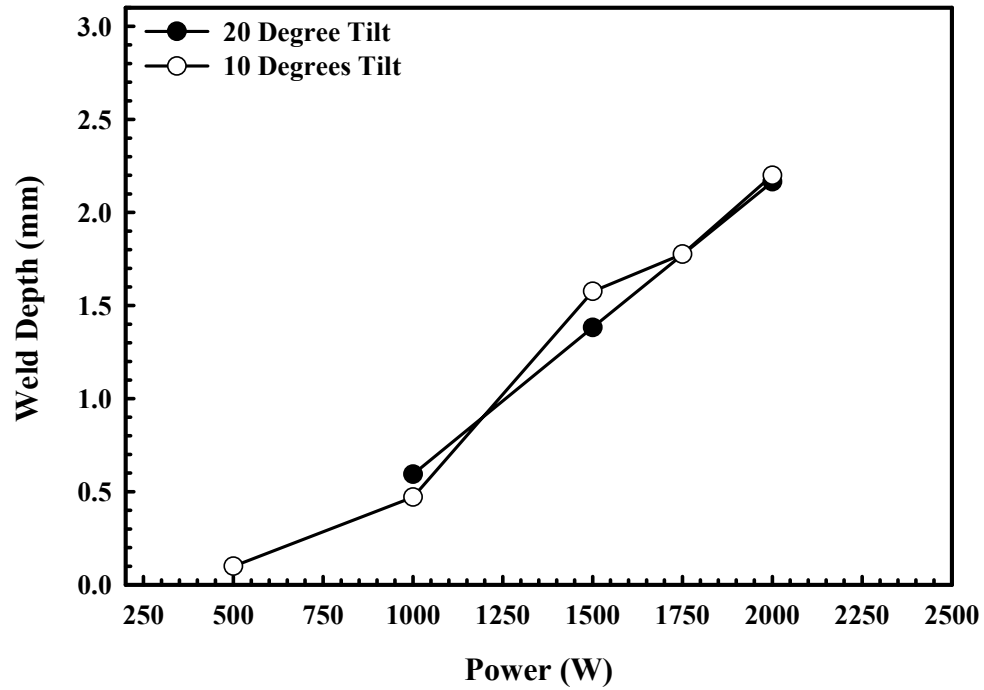


Figure 10. Plot of the measured weld depth as a function of power for tantalum samples welded with He shielding gas, at a travel speed of 30 in/min, and tilt angles of 10 and 20 degrees.

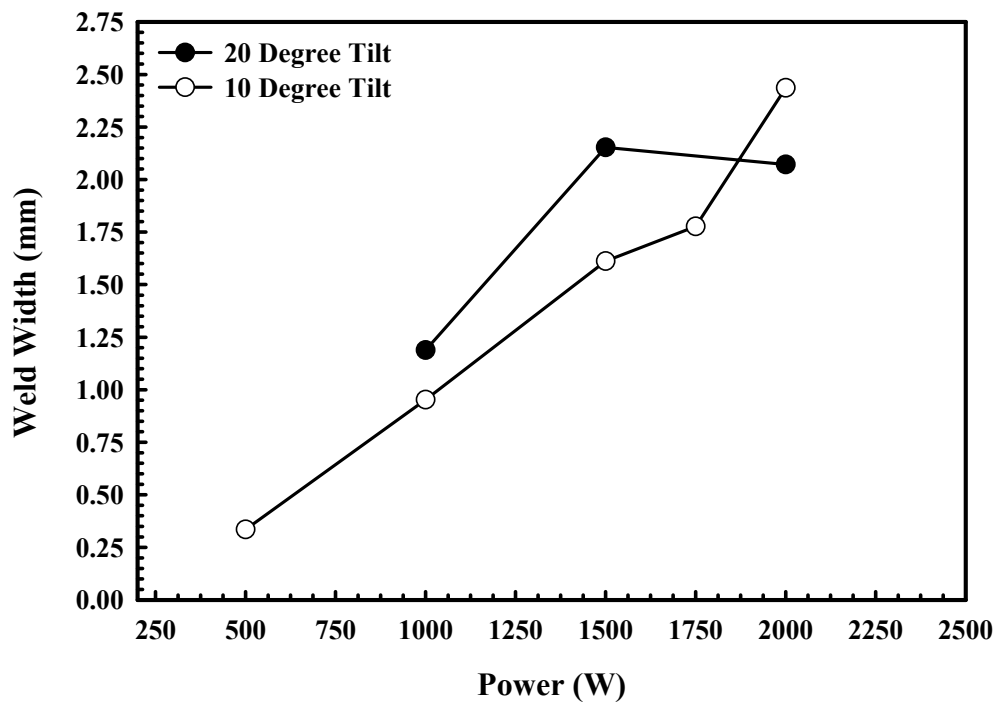


Figure 11. Plot of the measured weld width as a function of power for tantalum samples welded with He shielding gas, at a travel speed of 30 in/min, and tilt angles of 10 and 20 degrees.

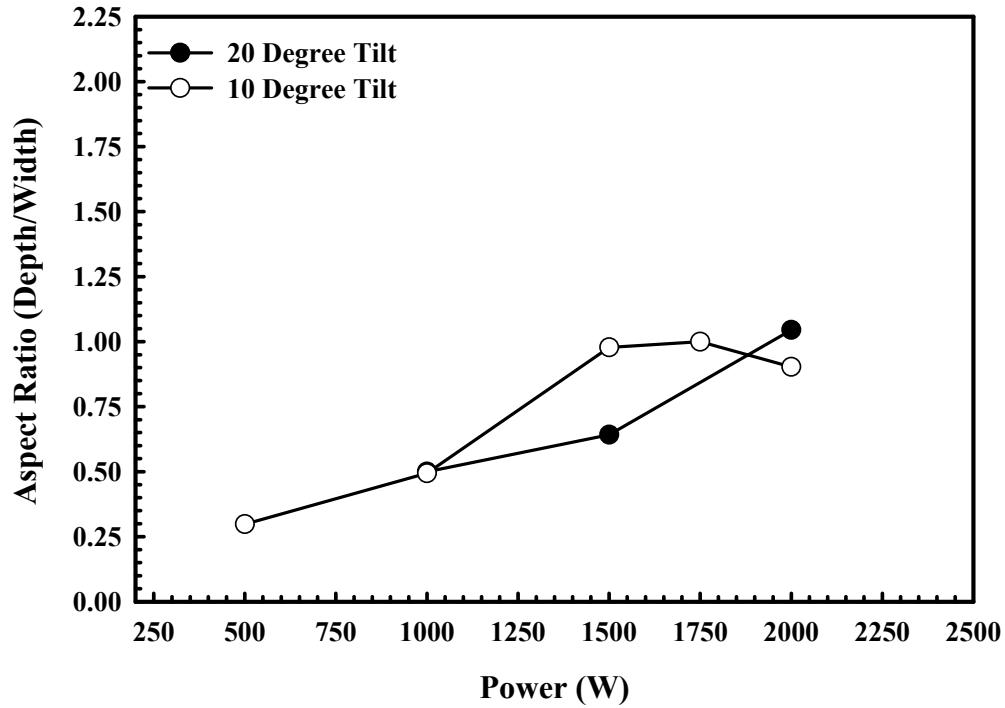


Figure 12. Plot of the aspect ratio (depth/width) as a function of power for tantalum samples welded with He shielding gas, at a travel speed of 30 in/min, and tilt angles of 10 and 20 degrees.

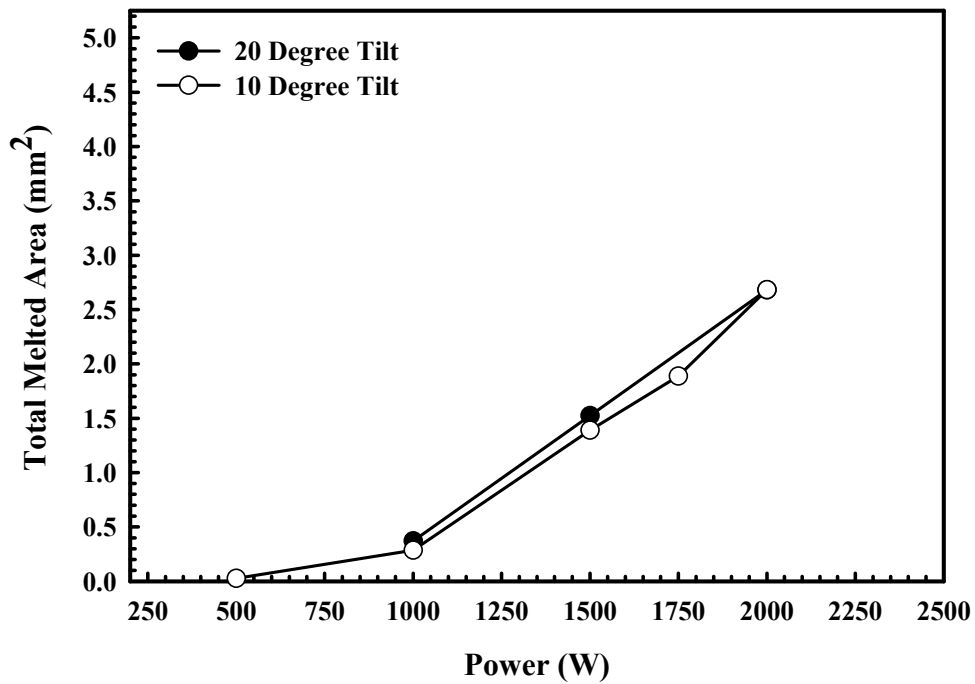


Figure 13. Plot of the total melted area as a function of power for tantalum samples welded with He shielding gas, at a travel speed of 30 in/min, and tilt angles of 10 and 20 degrees.

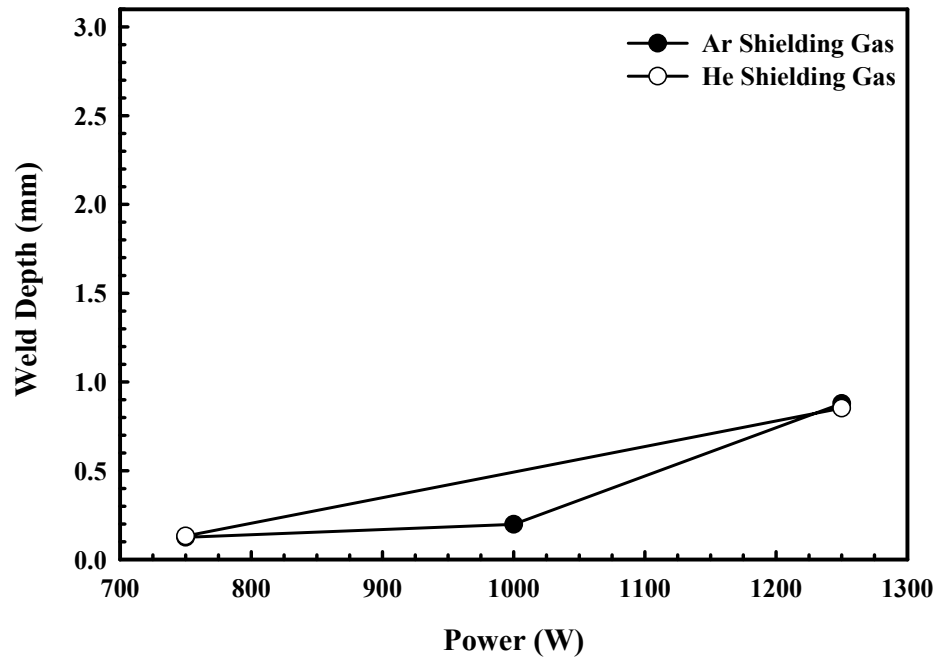


Figure 14. Plot of the measured weld depth as a function of power for tantalum samples welded with helium and argon shielding gases, at a travel speed of 45 in/min, and a tilt angle of 10°. No melting is observed with a head tilt of 20° for powers up to 3 kW.

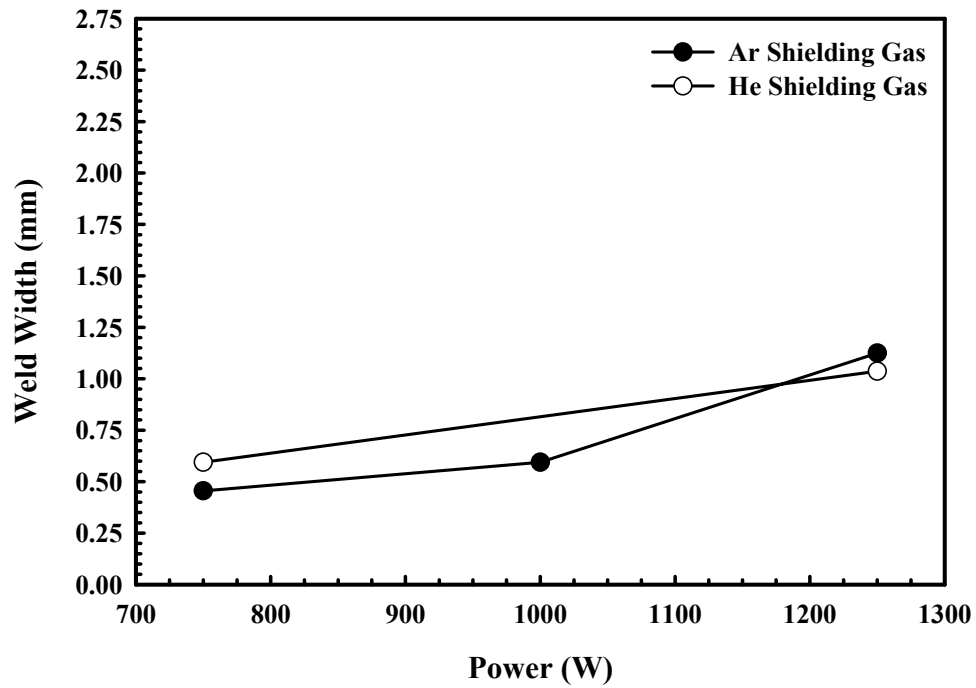


Figure 15. Plot of the measured weld width as a function of power for tantalum samples welded with helium and argon shielding gases at a travel speed of 45 in/min and a tilt angle of 10°. No melting is observed with a head tilt of 20° for powers up to 3 kW.

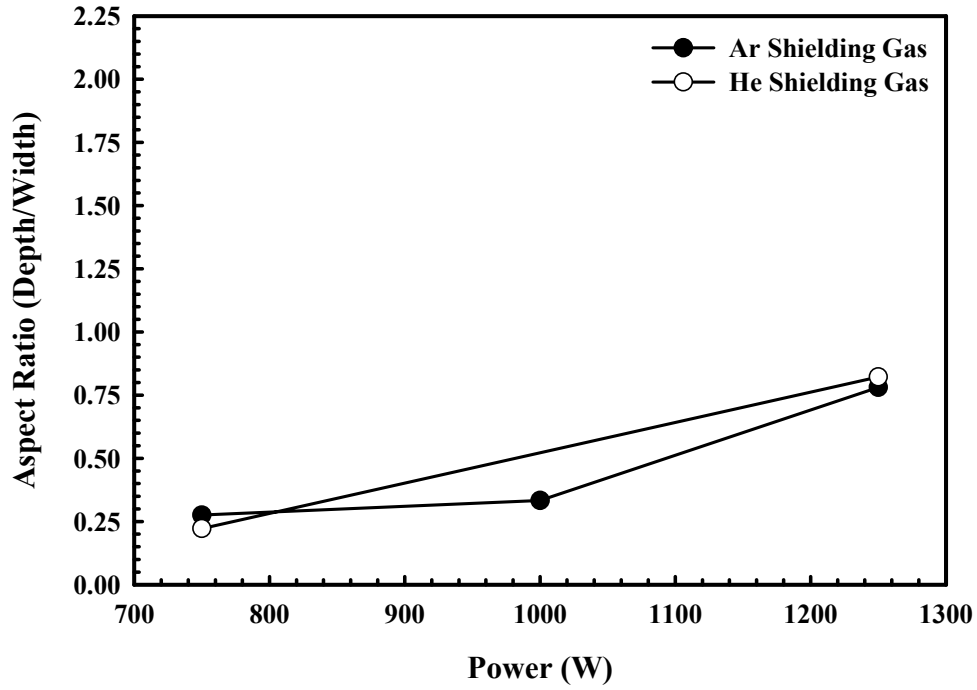


Figure 16. Plot of the aspect ratio (depth/width) as a function of power for tantalum samples welded with both helium and argon shielding gases at a travel speed of 45 in/min, and a tilt angle of 10°. No melting is observed with a head tilt of 20° for powers up to 3 kW.

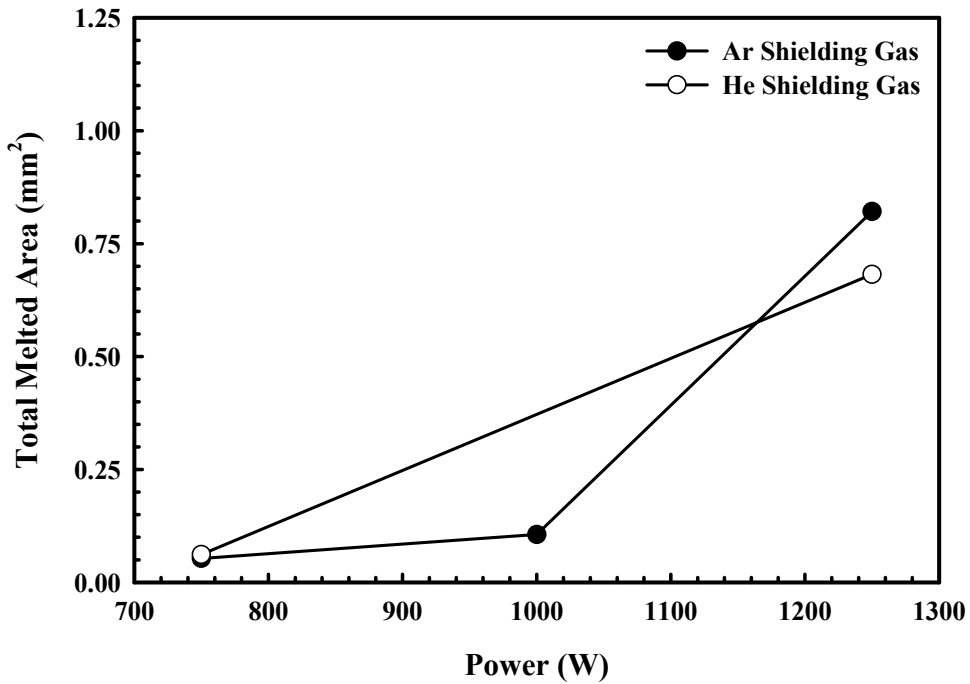
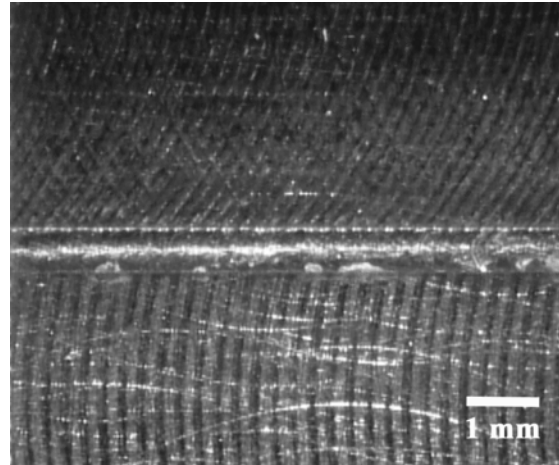
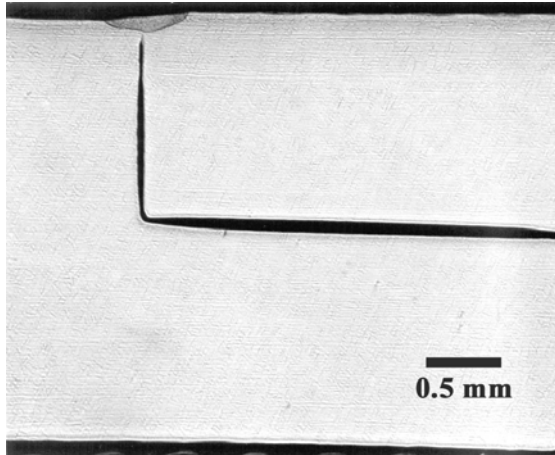


Figure 17. Plot of the total melted area as a function of power for tantalum samples welded with both helium and argon shielding gases at a travel speed of 45 in/min and a tilt angle of 10°. No melting is observed with a head tilt of 20° for powers up to 3 kW.

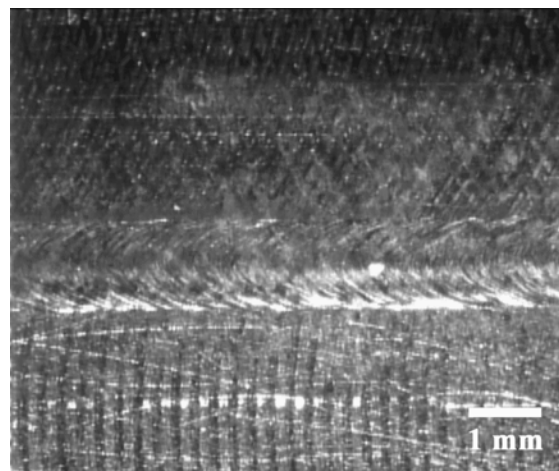
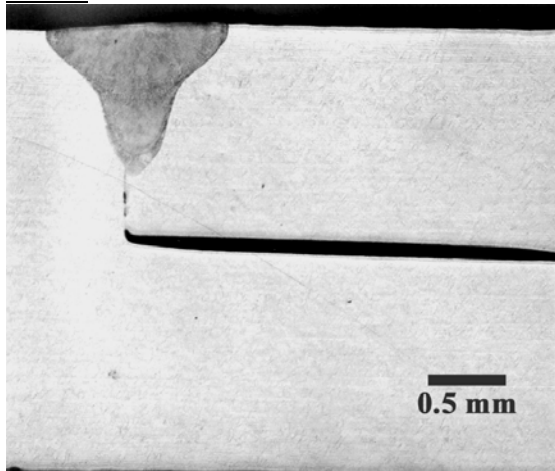
Appendix I. Micrographs of Weld Cross Sections and Top Surfaces for 21-6-9 Stainless Steel Welds.

He Shielding Gas, 45 in/min Travel Speed

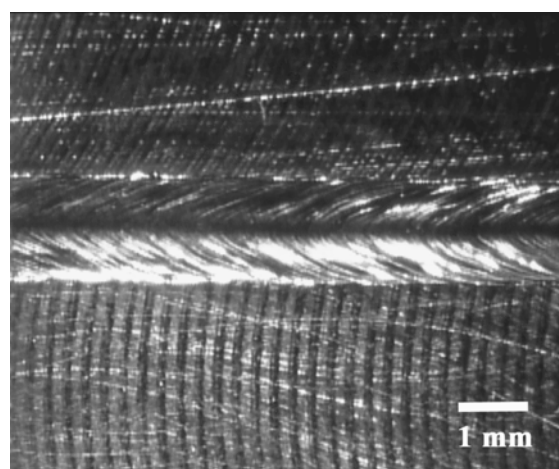
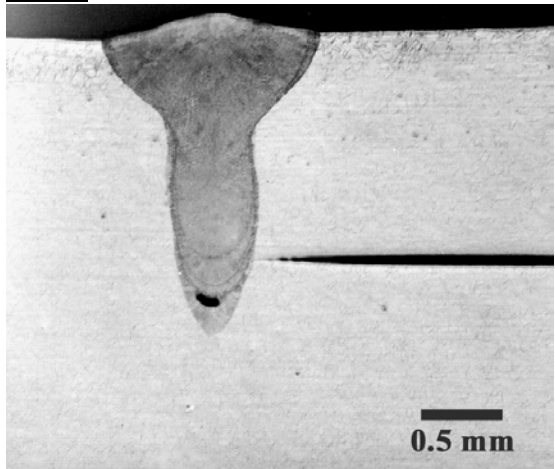
Power: 250 W



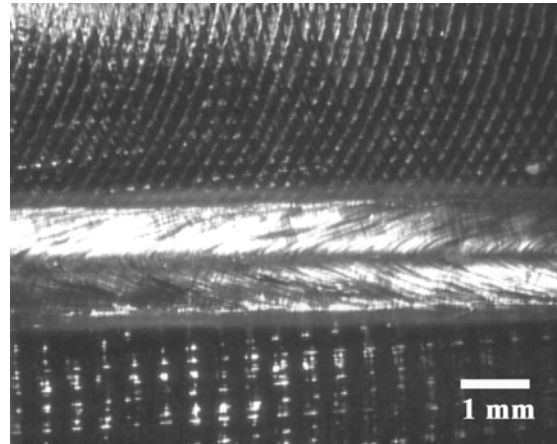
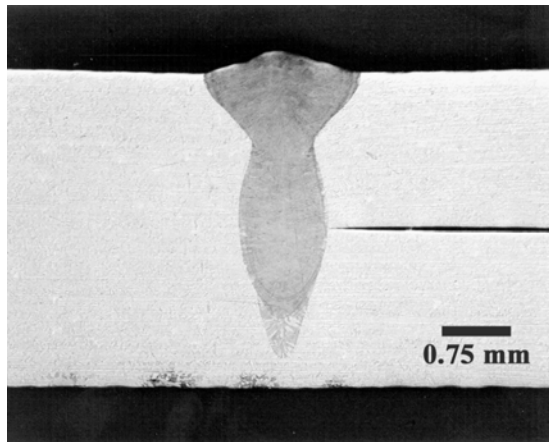
Power: 500 W



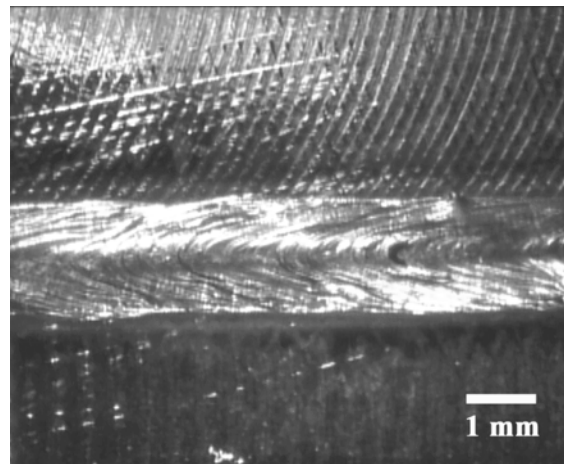
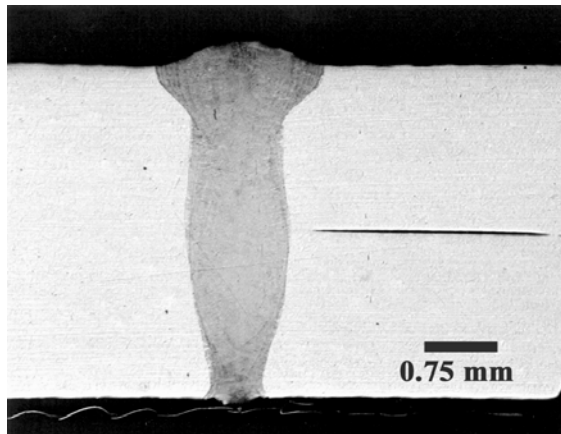
Power: 750 W



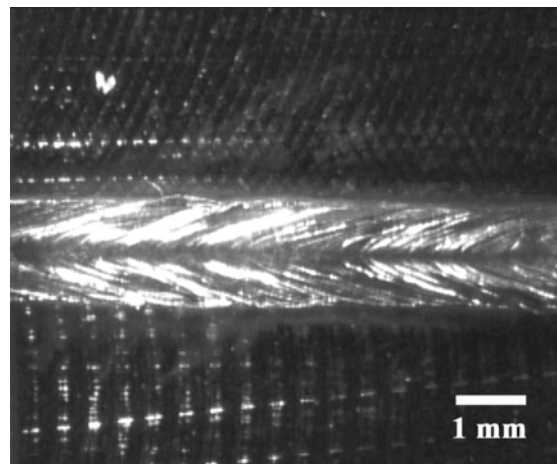
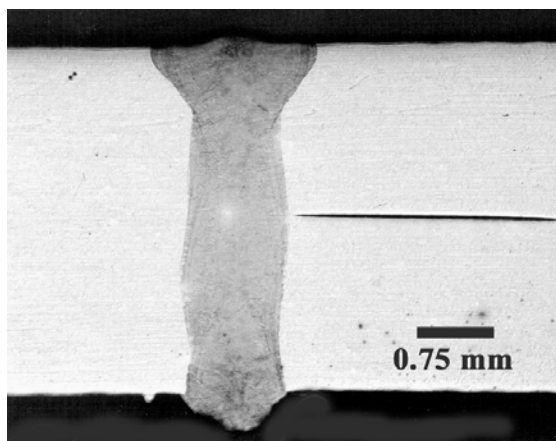
Power: 1000 W



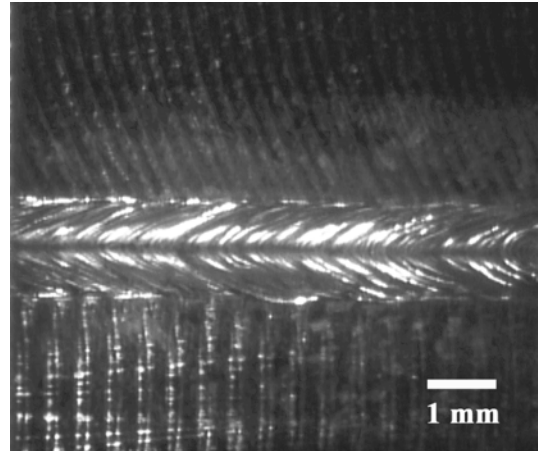
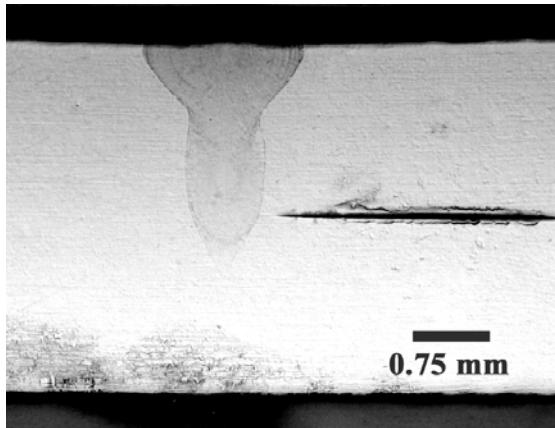
Power: 1250 W



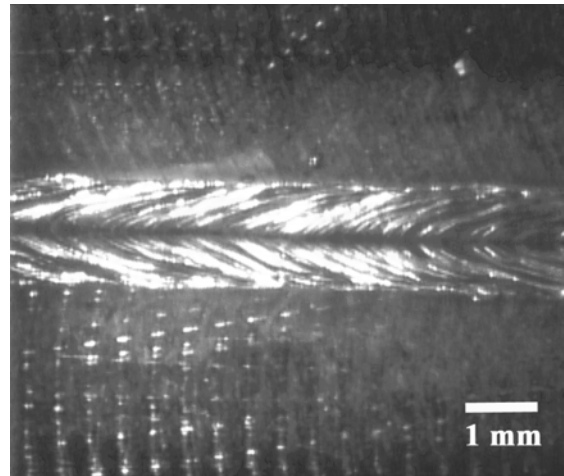
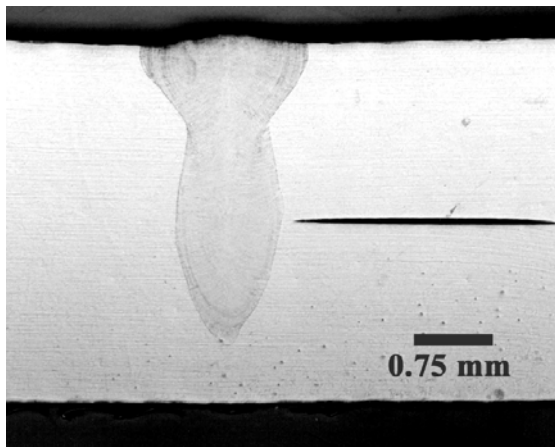
Power: 1500 W



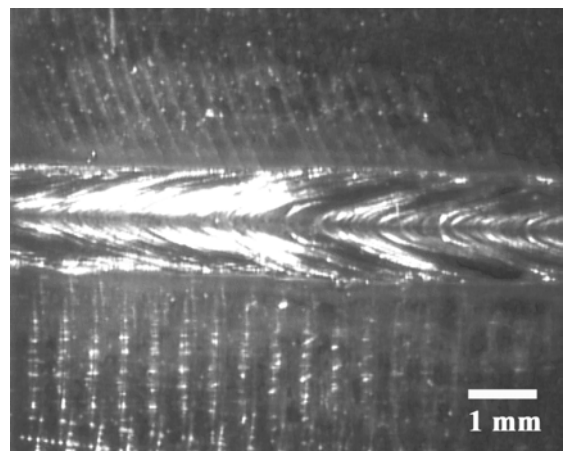
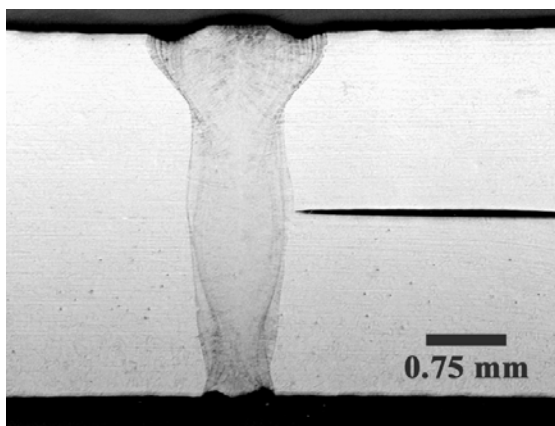
Ar Shielding Gas, 45 in/min Travel Speed
Power: 750 W



Power: 1250 W



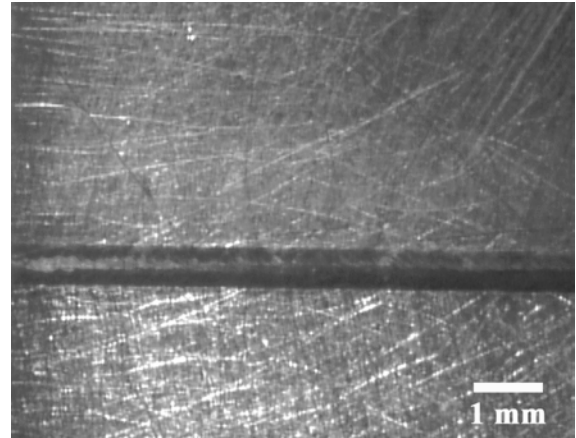
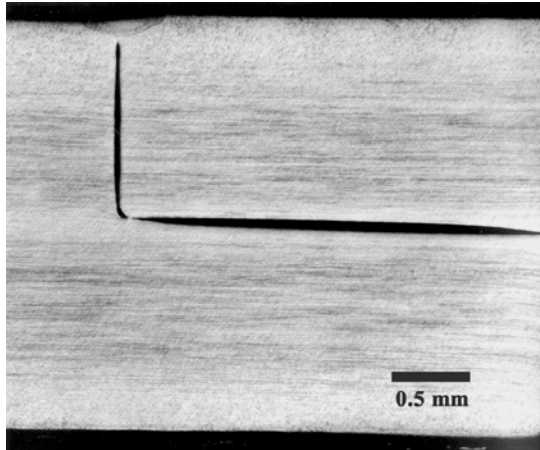
Power: 1500 W



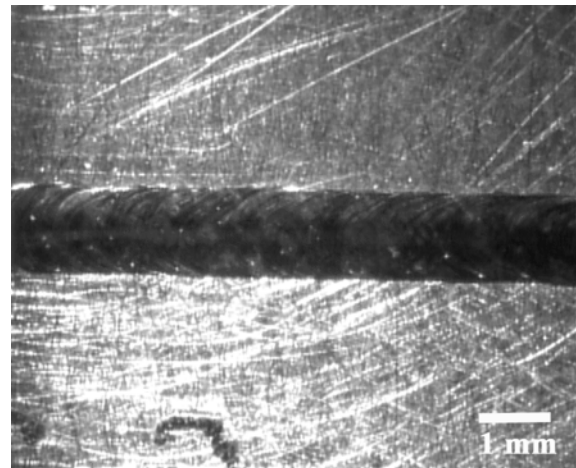
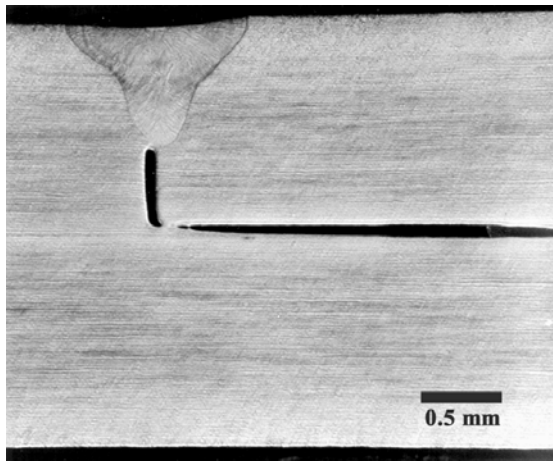
Appendix II. Micrographs of Weld Cross Sections and Top Surfaces for 304L Stainless Steel Welds.

He Shielding Gas, 45 in/min Travel Speed

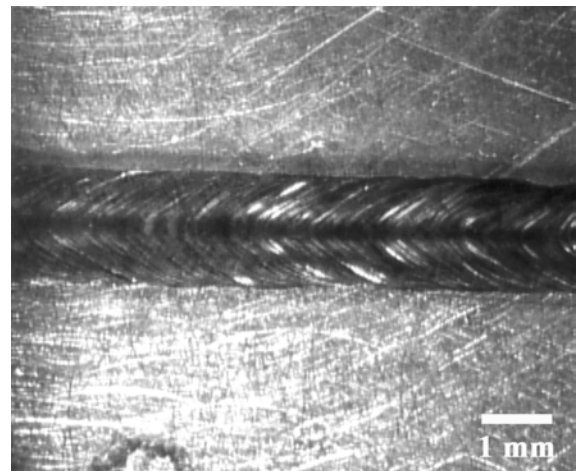
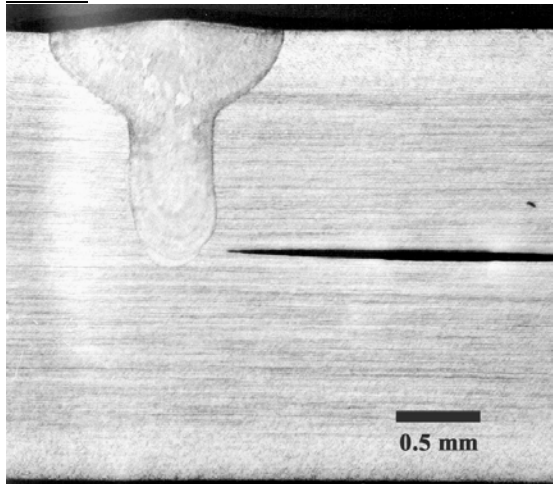
Power: 250 W



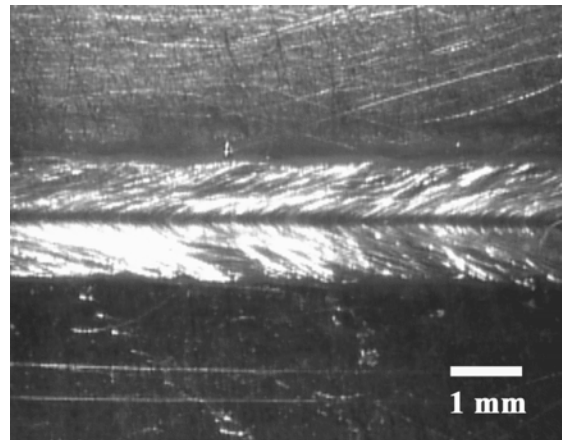
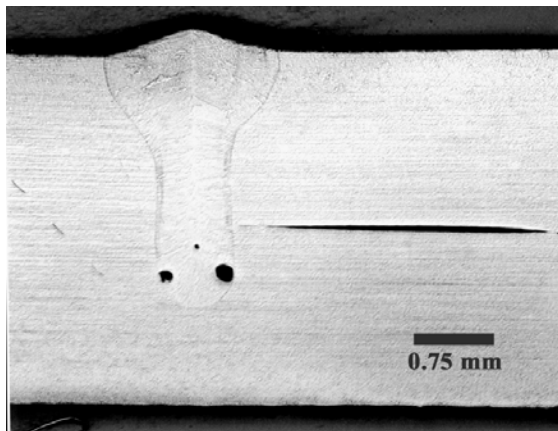
Power: 500 W



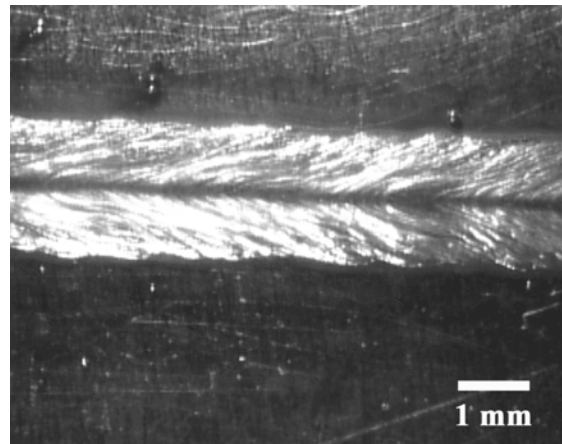
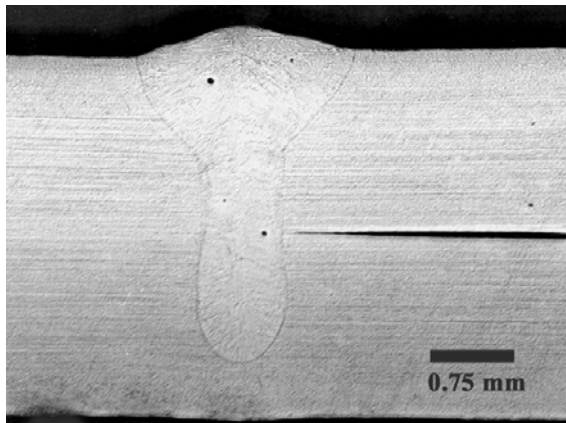
Power: 750 W



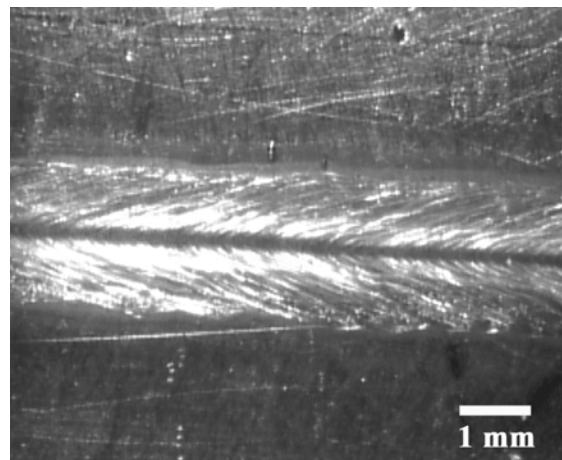
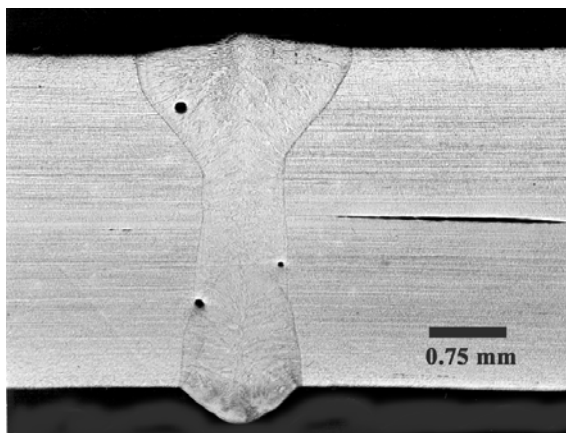
Power: 1000 W



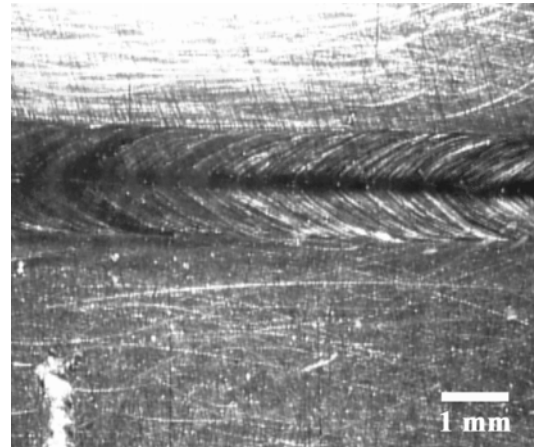
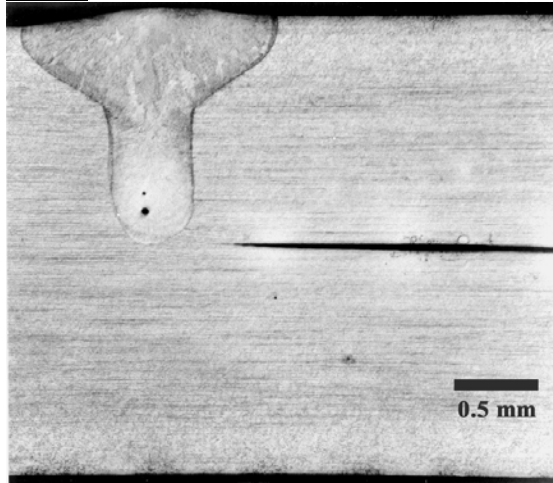
Power: 1250 W



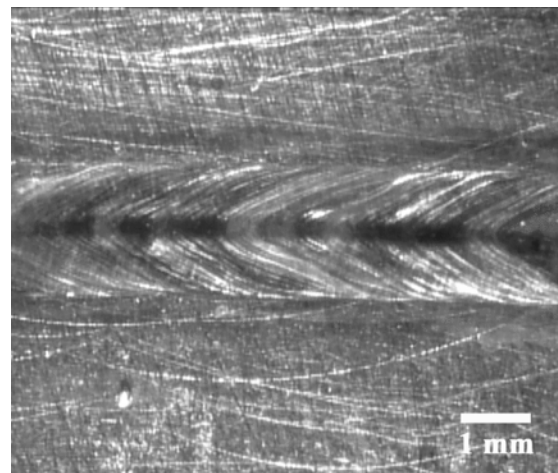
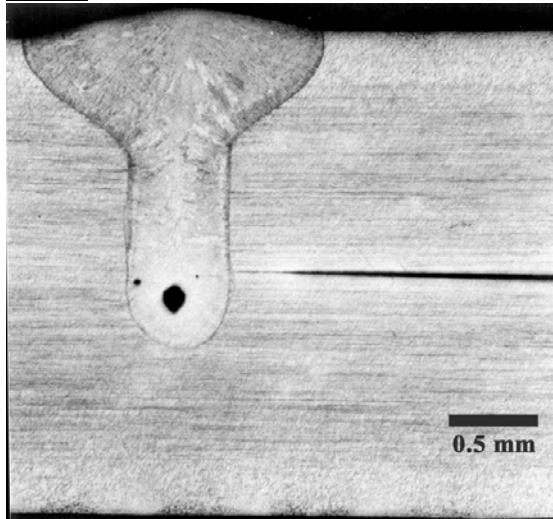
Power: 1500 W



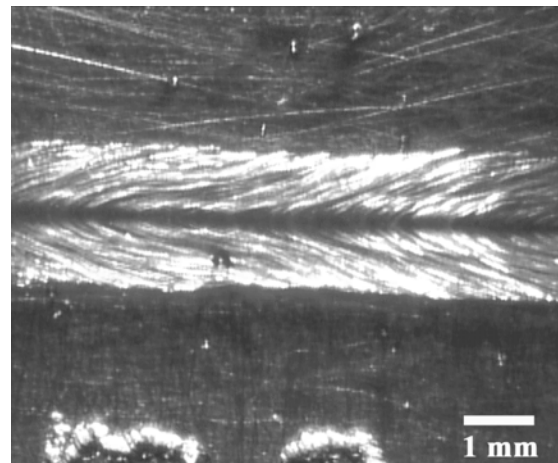
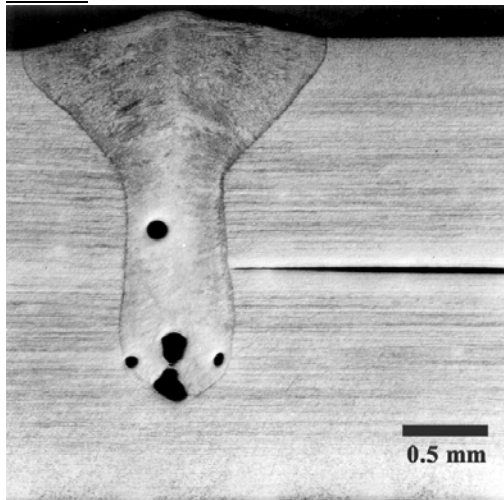
Ar Shielding Gas, 45 in/min Travel Speed
Power: 750 W



Power: 1000 W

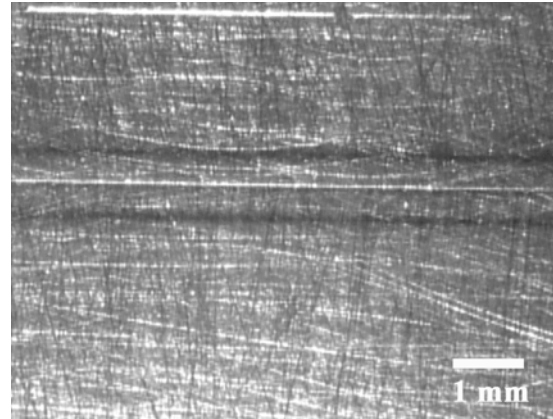
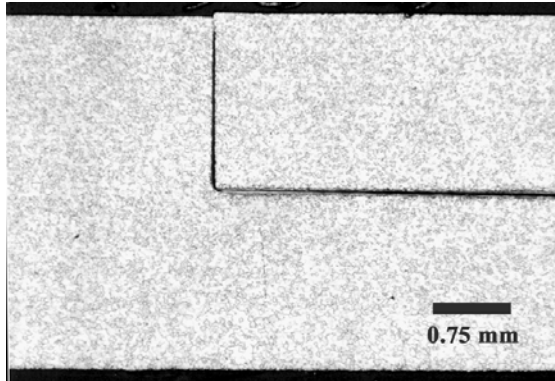


Power: 1250 W

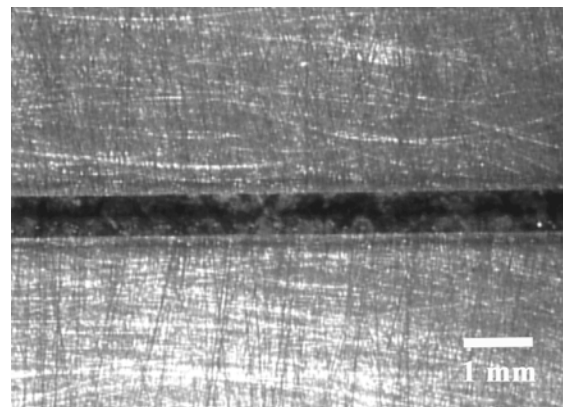
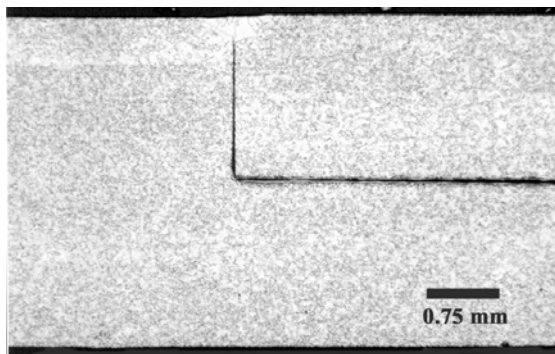


Appendix III. Micrographs of Weld Cross Sections and Top Surfaces for Vanadium Welds.

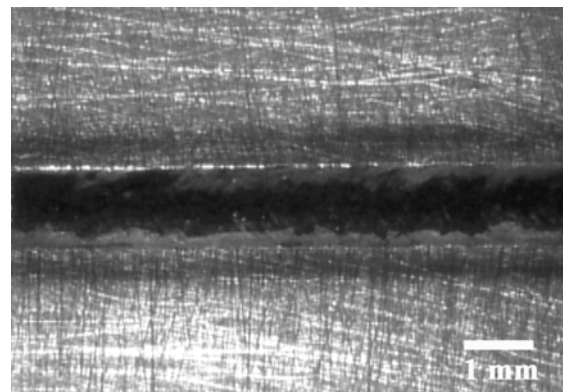
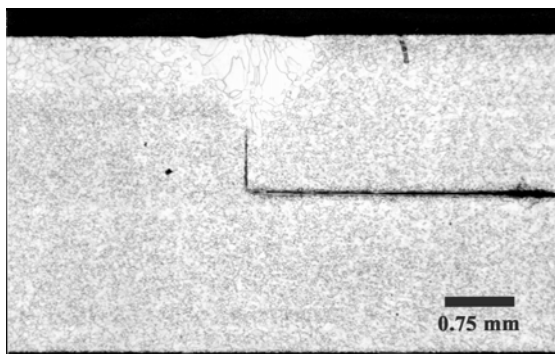
He Shielding Gas, 45 in/min Travel Speed
Power: 250 W



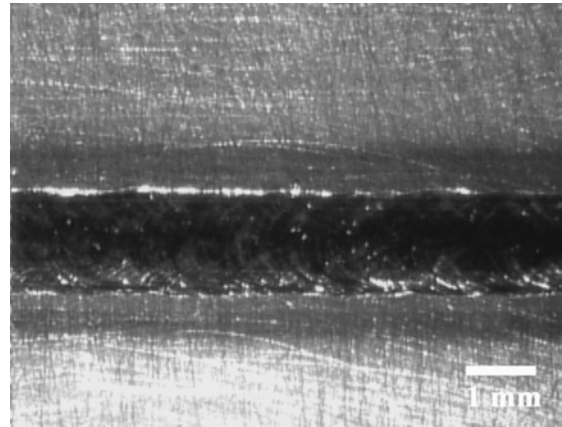
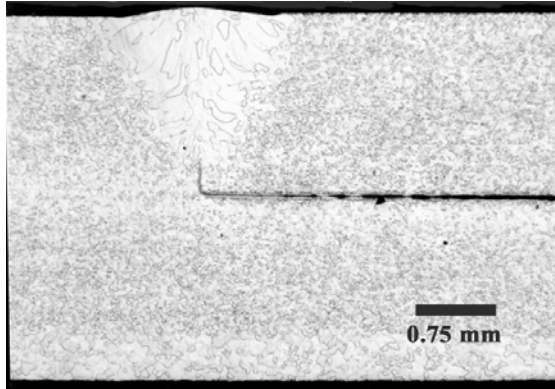
Power: 500 W



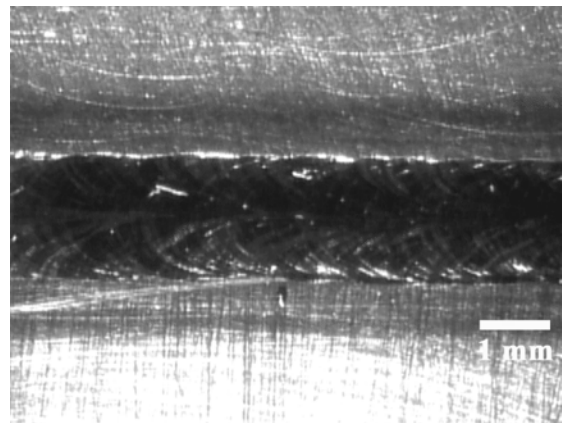
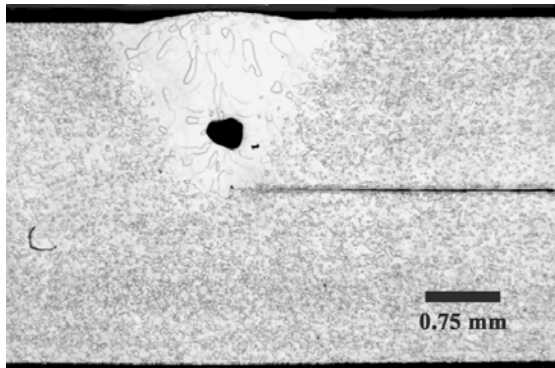
Power: 750 W



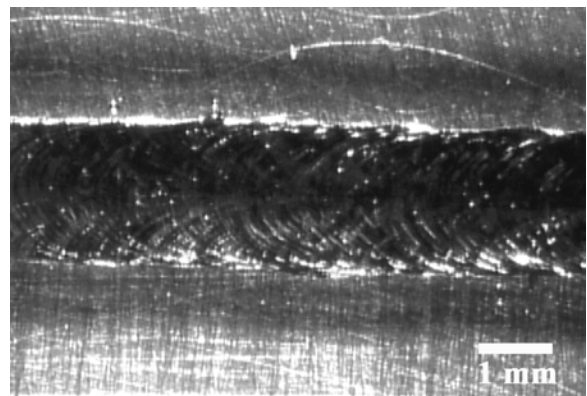
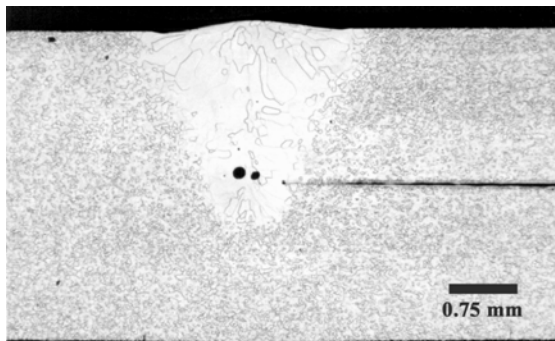
Power: 1000 W



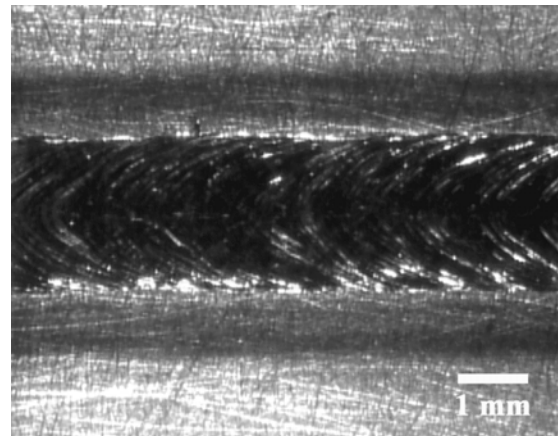
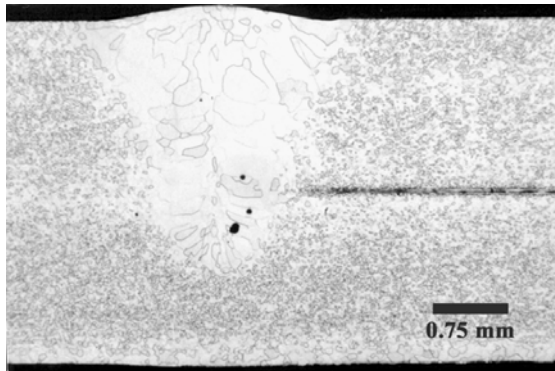
Power: 1250 W



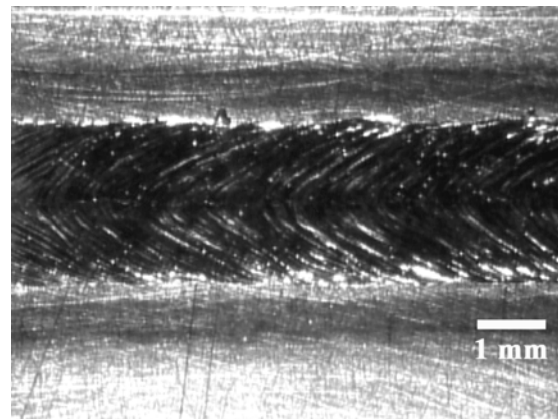
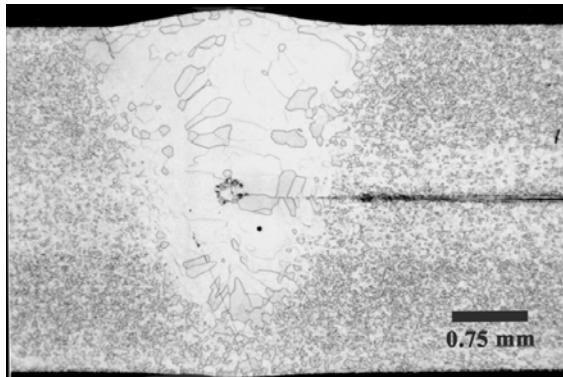
Power: 1500 W



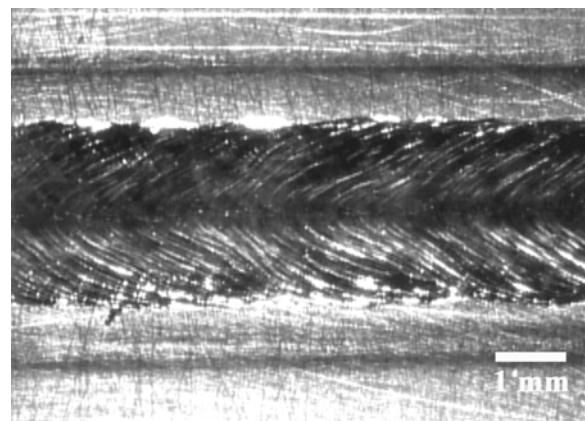
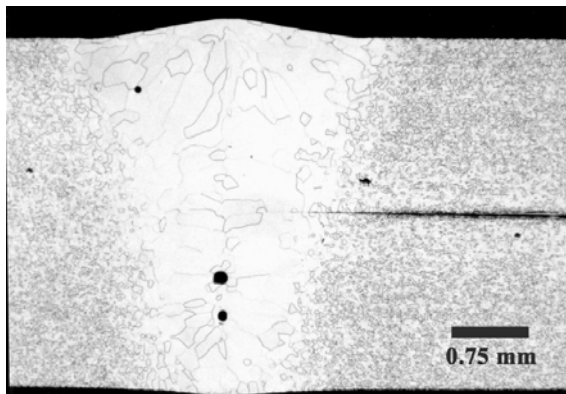
Power: 1750 W



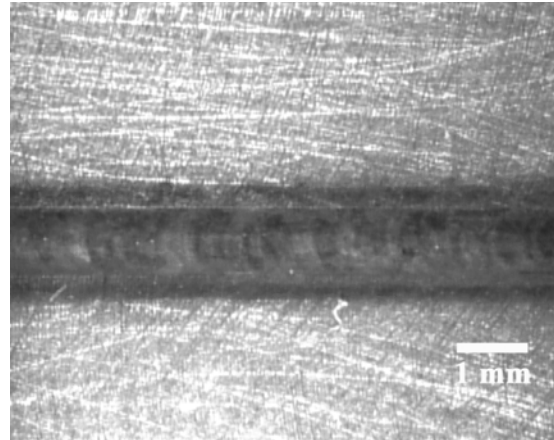
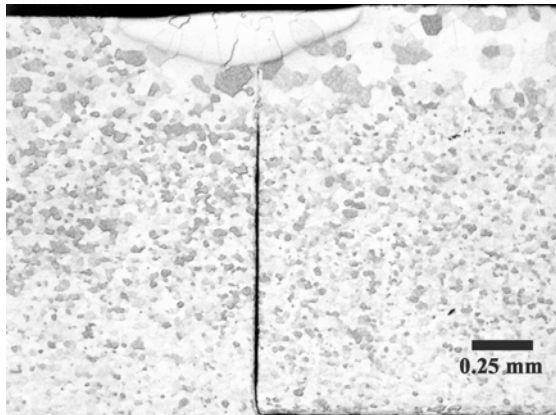
Power: 2000 W



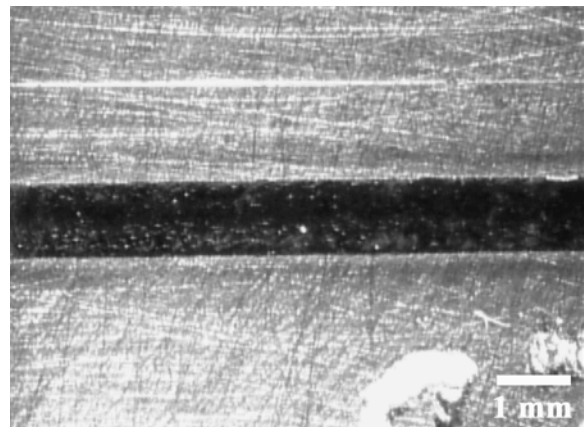
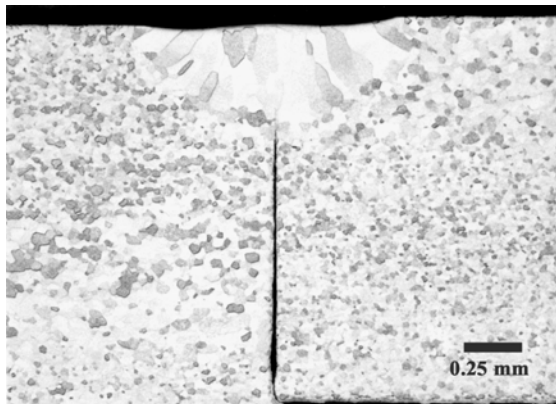
Power: 2250 W



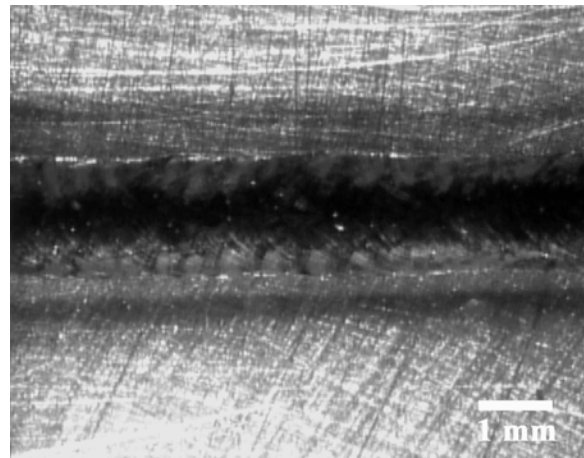
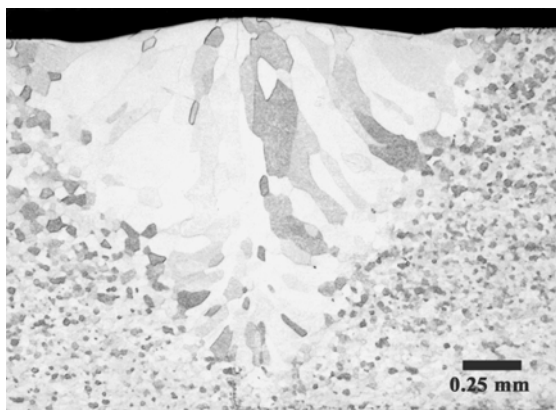
Ar Shielding Gas, 45 in/min Travel Speed
Power: 750 W



Power: 1000 W

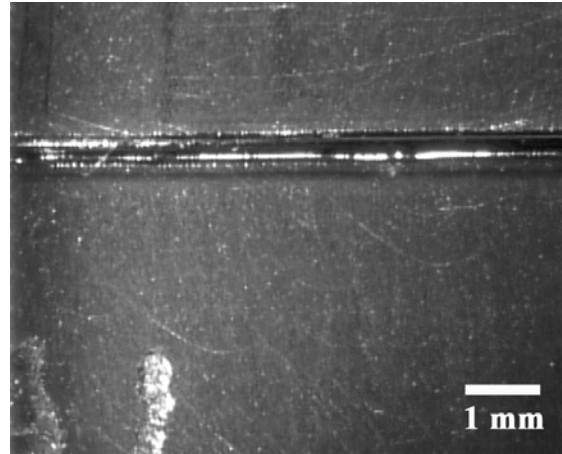
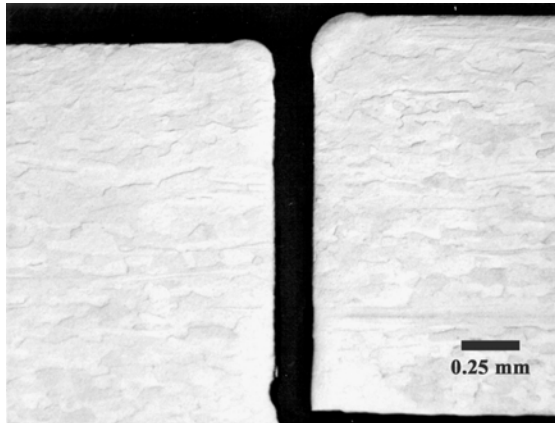


Power: 1250 W

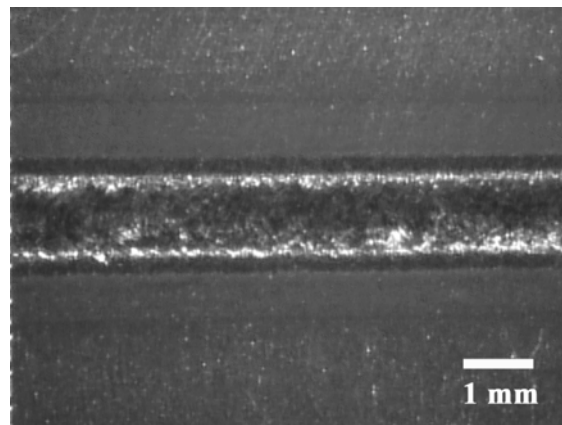
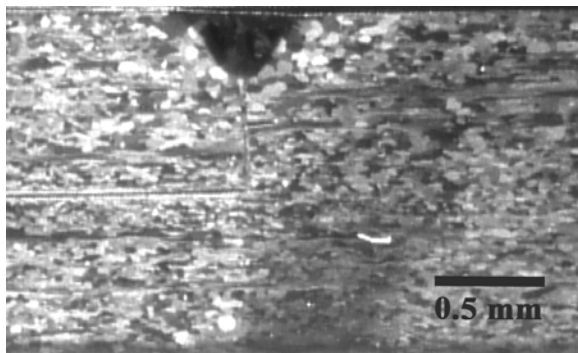


Appendix IV. Micrographs of Weld Cross Sections and Top Surfaces for Tantalum Welds.

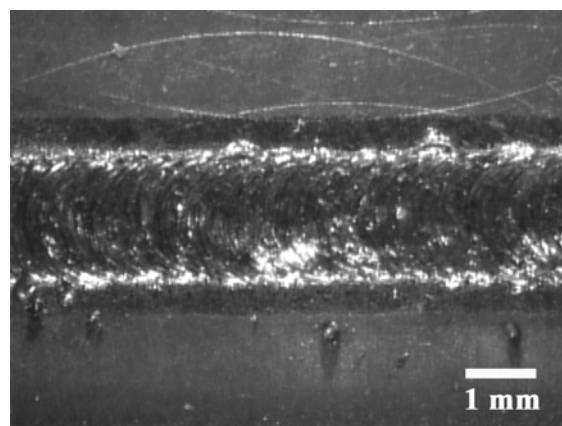
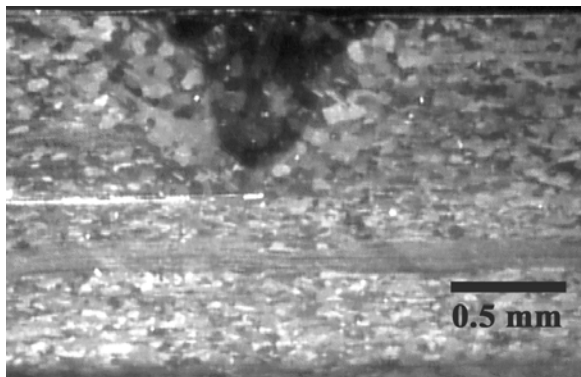
He Shielding Gas, 30 in/min Travel Speed, 20° Head Tilt
Power: 500 W



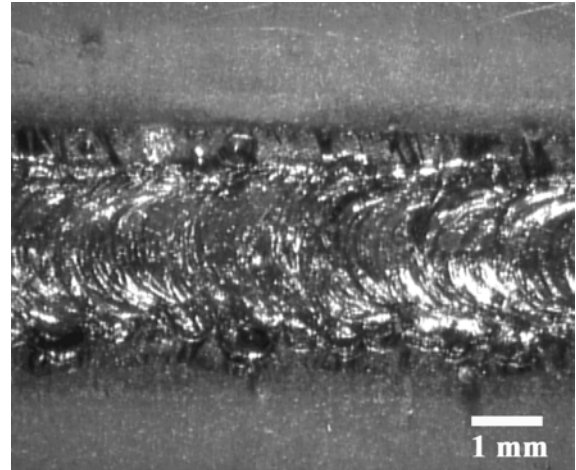
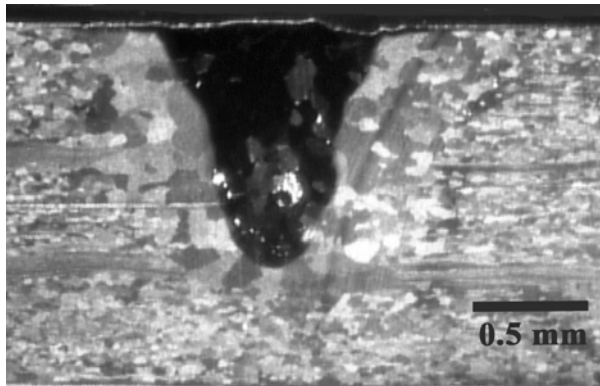
Power: 1000 W



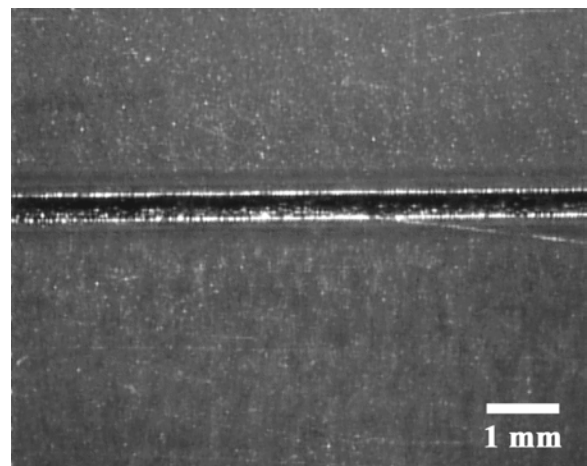
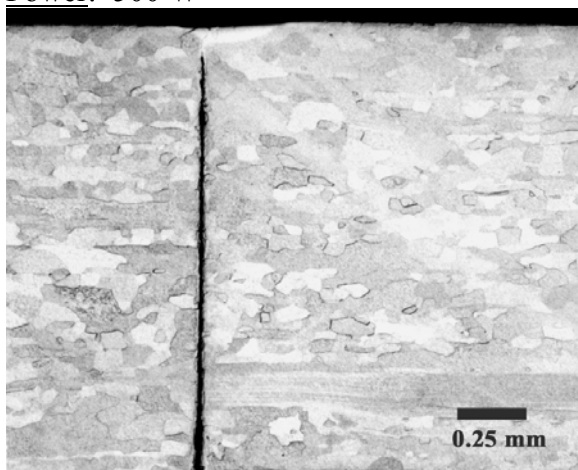
Power: 1500 W



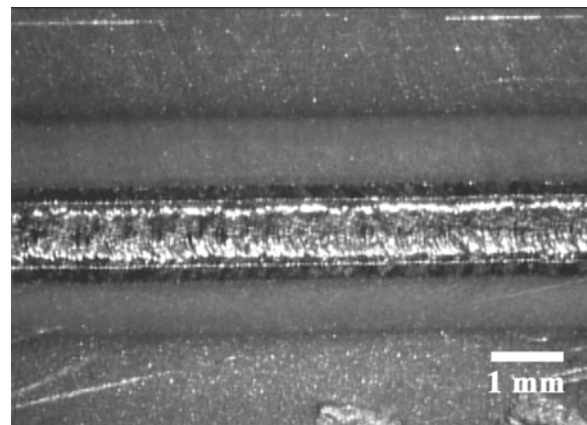
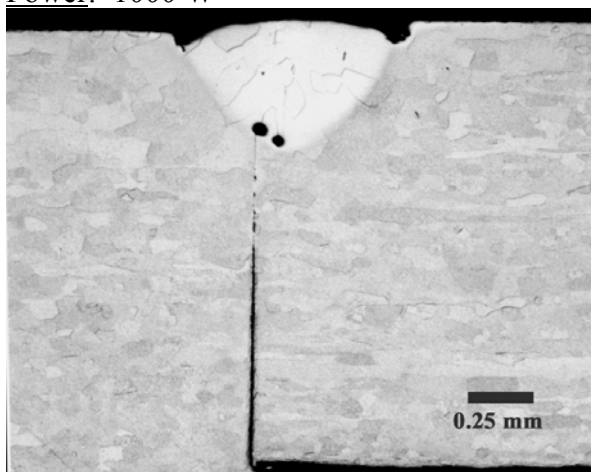
Power: 2000 W



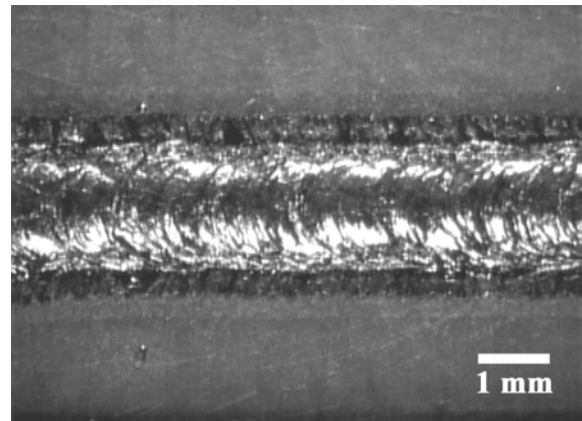
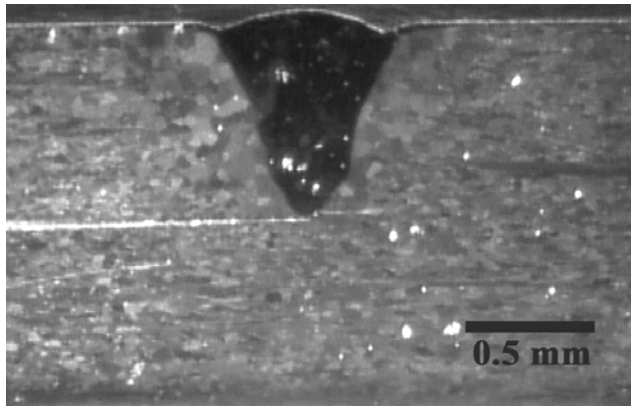
He Shielding Gas, 30 in/min Travel Speed, 10° Head Tilt
Power: 500 W



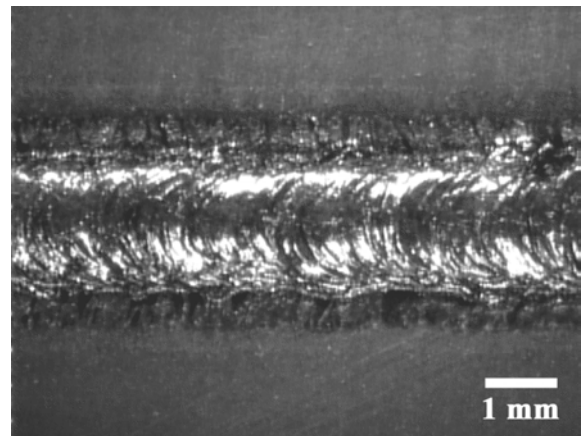
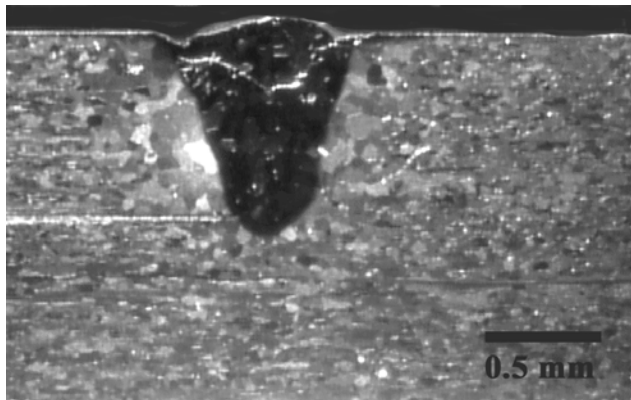
Power: 1000 W



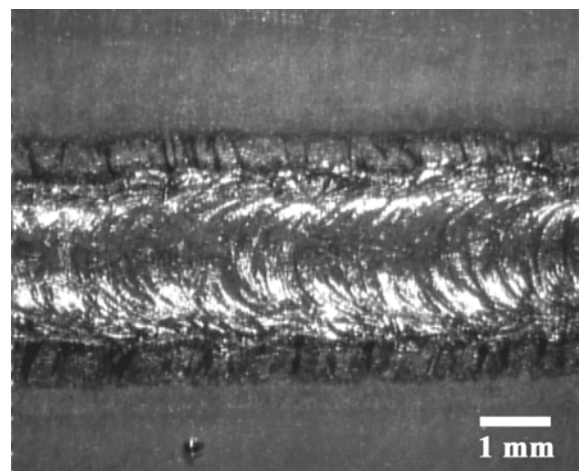
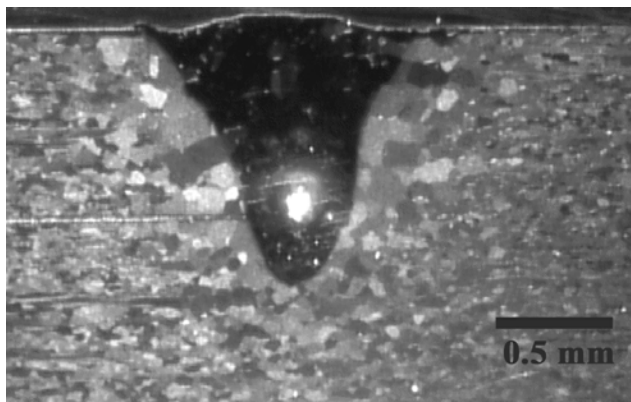
Power: 1500 W



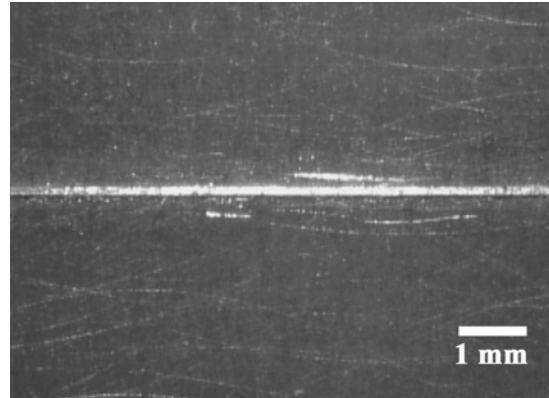
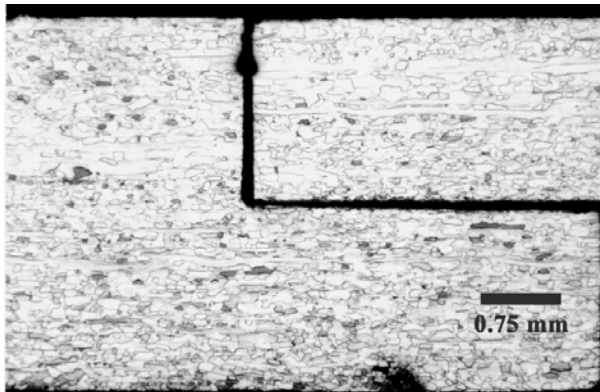
Power: 1750 W



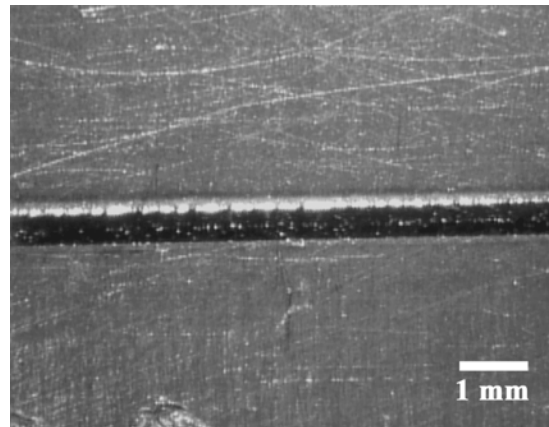
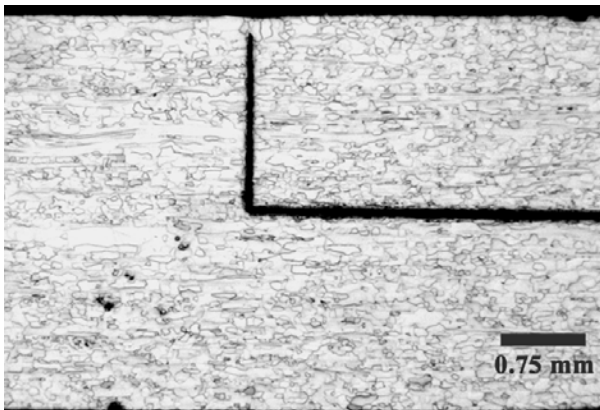
Power: 2000 W



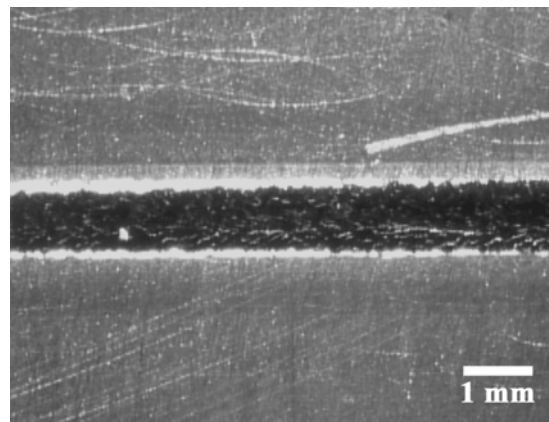
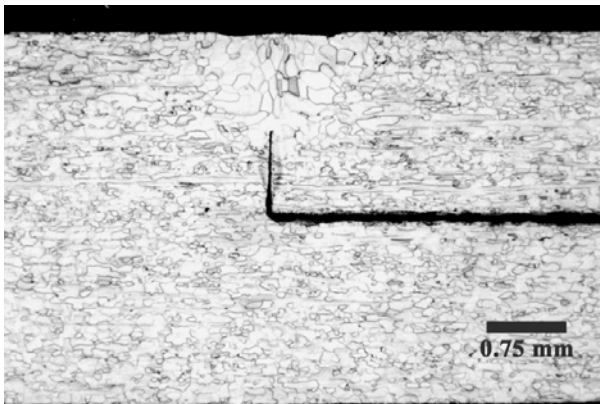
He Shielding Gas, 45 in/min Travel Speed, 10° Head Tilt
Power: 250 W



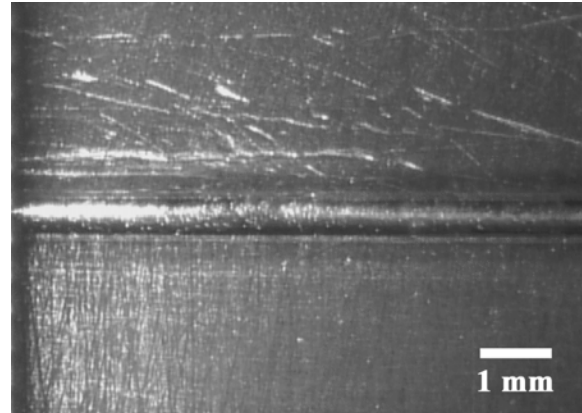
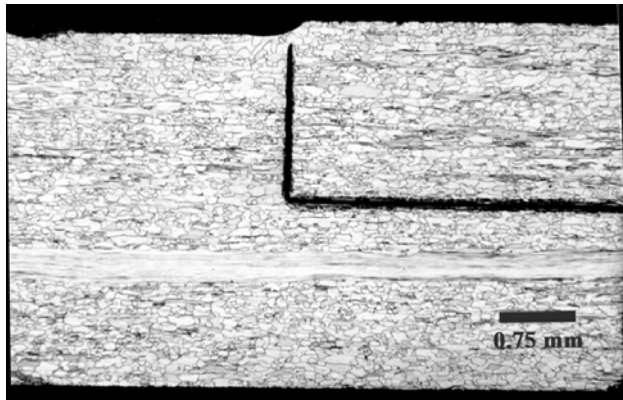
Power: 750 W



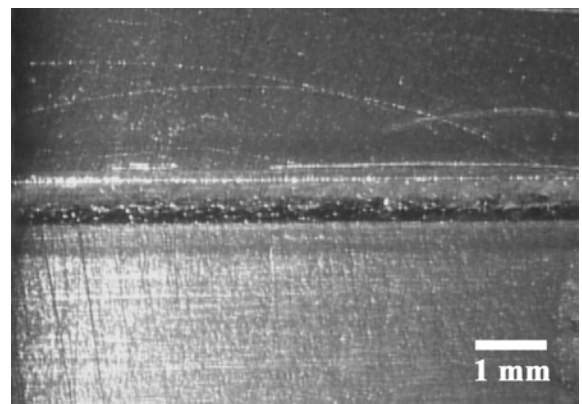
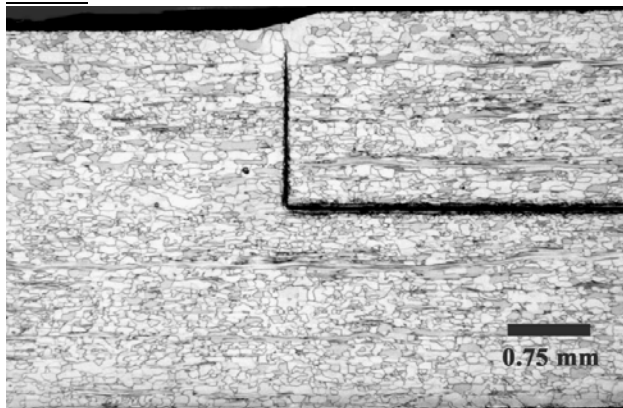
Power: 1250 W



Ar Shielding Gas, 45 in/min Travel Speed, 10° Head Tilt
Power: 750 W



Power: 1000 W



Power: 1250 W

